Investigation of Quenched-in Vacancies in Pure Aluminium and the Precipitation in Al-Zn-Mg Alloys

von

Meng Liu

Diplomarbeit in Physik

angefertigt am

Helmholtz-Institut für Strahlen- und Kernphysik

vorgelegt der

Mathematisch-Naturwissenschaftlichen Fakultät

der Rheinischen Friedrich-Wilhelms-Universität Bonn

im Januar 2010

Ich versichere, dass ich diese Arbeit selbständig verfasst und keine adneren als die angegebenen Quellen und Hilfsmittel benutzt sowie die Zitate als solche Kenntlich gemacht habe.

Referent: Prof. Dr. K. Maier
Korrreferent: Priv. Doz. Dr. R. Vianden

Contents

Chapter 1
Introduction

Aluminium and its alloys are widely applied in our daily lives as packaging, engineering, transportation and construction material due to their unique properties, namely light weight, high strength, corrosion resistance and recyclability.

In metals the concentration of thermal vacancies increases with temperature and a considerable fraction of thermal vacancies is frozen inside the material by a quenching process. Information about these quenched-in vacancies is hard to access since they diffuse to the surface, grain boundaries or dislocations and thus disappear at room temperature in few minutes. However, a vacancy reference in pure aluminium is desired nevertheless. Therefore, an optimized quenching technique is used in this study to improve the quenching rate, utilizing e.g. a cooled HCl solution as quenching medium, in order to freeze vacancies more effectively. Based on this quenching method a vacancy reference in pure aluminium is obtained using positron annihilation spectroscopy including Doppler Broadening Annihilation Radiation (DBAR) spectroscopy and Positron Lifetime Spectroscopy (PLS) techniques, which are especially suitable for the investigation of open volume defects like vacancies. In addition theoretical calculation will be compared to the experimental results.

The strength of aluminium alloys depend not only on the components of the specific alloys, but also on the employed heat treatments and manufacturing processes. An example is the age-hardenable, quaternary Al-Zn-Mg-Cu alloy of the AA 7xxx series, which is widely used as a structural material in aerospace and automotive industries. By applying Doppler Broadening Annihilation Radiation spectroscopy, information about solute concentration around vacancies and / or their relaxation was obtained for AA 7075 under different conditions. Particularly, according to literature, it is believed that η′ precipitates formed by aging the alloy at 130℃ for 3 hours, are dominantly responsible for the strengthening.

Moreover, X-ray Absorption Spectroscopy (XAS) experiments were carried out at BESSY at the 7T-MPW-magS beamline by measuring the K-edge XANES of the main alloying element Zn from AA 7075 samples. Comparison between experimental and numerical calculation results allows obtaining complementary information about the local structure around Zn-atoms. Thus, in this study the AA 7075 is tackled from both relevant perspectives, viz. vacancy and solute related.

Chapter 2
Theoretical Fundamentals

2.1. Defects in Crystal

The ideal arrangement of atoms in crystalline solids is a periodic structure, but in reality they are not perfectly arranged. The regular structure is disturbed by crystal defects like point defects, line defects and planar defects according to their geometry. The existence of defects has big influence on the physical properties of the material, therefore they are widely investigated by different techniques such as positron annihilation spectroscopy which has been applied in this study.

2.1.1. Point Defects

Point defects are the simplest type of defect. An atom of the lattice structure is missing or is in an irregular position. Typical point defects include vacancies (Schottky defect), interstitials, Frenkel pairs and impurities, which are illustrated below [web1]:

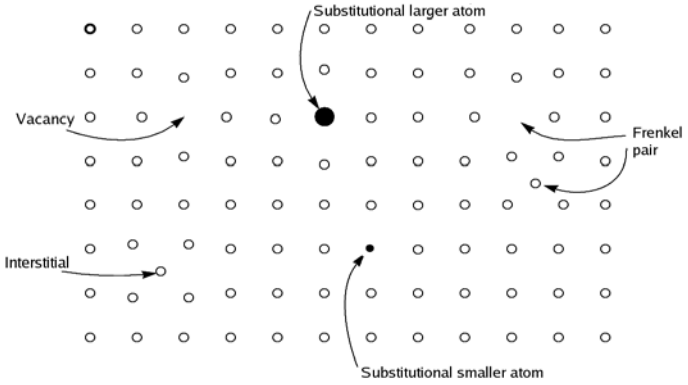

Fig. 2.1: Schematic illustration of some simple point defect types.

Atoms change their positions frequently due to thermal vibration. Randomly they are able to move to the surface area in case of sufficient kinetic energy and as a result unoccupied lattice sites are left behind, namely vacancies. Interstitials are created once the sites in the crystal structure are occupied by some atoms, where actually no atom should be. A pair of a vacancy and an interstitial forms the so called Frenkel pair. In reality materials are never 100% pure and those atoms which differ from the bulk atoms are impurities. In general there are two types of impurity atoms, viz. substitutional impurity and interstitial impurity atoms. The former one is an impurity atom which replaces a bulk atom in the lattice (substitutional atom in Fig. 2.1) and the latter one fits itself into the space between the bulk atoms (interstitial atom in Fig. 2.1).

2.1.2. Line Defects

Line defects or dislocations are one-dimensional linear defects for which atomic planes are misaligned in the crystal lattice. Historically the concept of dislocations was introduced in order to explain the low value of experimentally observed critical shear stress for rigid displacements. This means that instead of the movement of the entire crystal the dislocation line will move inside the crystal under small shear stresses. After a dislocation line has left the crystal and disappeared, part of the crystal is moved relative to the rest, thus the rigid deformation is achieved. In general, dislocations play an important role for the mechanical, electrical and optical properties of crystals. There are two principal kinds of dislocations, viz. the edge dislocation and the screw dislocation, as shown in Fig. 2.2 [Web2]:

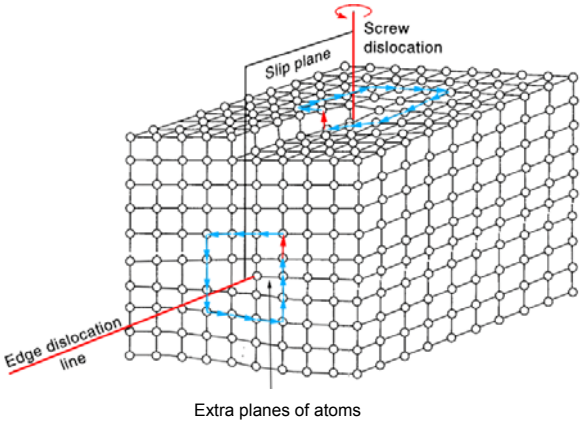

Fig. 2.2: Edge dislocation and screw dislocation, the Burgers vector is indicated by red arrow.

Edge dislocations refer to the structure illustrated in Fig. 2.2. The periodical structure around them is interrupted by the knife-like extra half plane of atoms inserted between other crystal planes. The adjacent planes are then no longer planar but distorted instead, lattice strain (distortion) is thus introduced in the vicinity of dislocations. The direction and magnitude of lattice distortions caused by dislocations is quantified by the so-called Burgers vector. For edge dislocations the Burgers vector is perpendicular to the dislocation line. In order to visualise the screw dislocations it is helpful to image cutting a crystal half through and slip one part against the other afterwards. The boundary from the cut is then called screw dislocation. In such a case the atomic planes form a spiral twist around the dislocation line. The Burgers vector is now parallel to the dislocation line. By positron annhilation techniques defects types from below can be investigated [Lrp]:

Defect type		size
Atomic vacancies		~ 0.1 nm
Dislocations		1nm-10mm
Voids		0.1nm-1mm

Table 2.1: Most suitable defects types for PAS method. Dislocations of the size 1nm-10nm are scaled with attached open-volume defects.

2.2. Aluminium and Aluminium Alloys

2.2.1. About Aluminium

As the most abundant metallic element in the Earth's crust (8wt% of the Earth's solid surface) aluminium is a member of group 3 in the periodic table with the symbol **Al** and atomic number 13. It was first produced by the Danish chemist Hans Christian Oersted in 1825. Aluminium is chemically too reactive to be found in nature as a free metal but in combination with other elements in compound form. The extreme difficulties to extract aluminium from those ores made pure aluminium more valuable than gold in the history until the Hall-Héroult process was developed. Nowadays the production of aluminium has increased from 1.5 million tons of the year 1950 to 33.7 million tons in 2008 worldwide to fulfill the enormous demand [Web3].

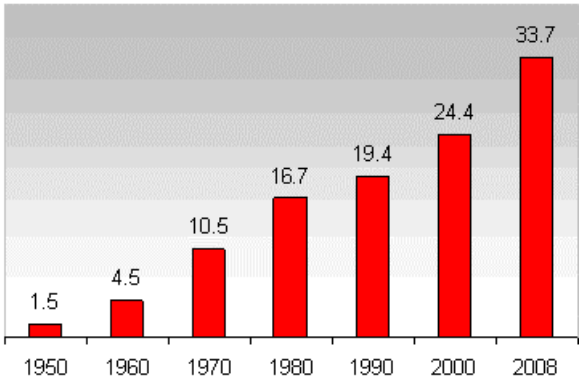

Fig. 2.3: The increase of worldwide production of primary aluminium in million metric tons.

The combination of unique properties such as light weight, high strength (alloyed with other elements), corrosion resistance makes aluminium a valuable stuff to be extensively used in our daily lives as packaging, engineering, transportation or construction material. Different usage of Aluminium from various countries are illustrated in the following Figure [Web4]:

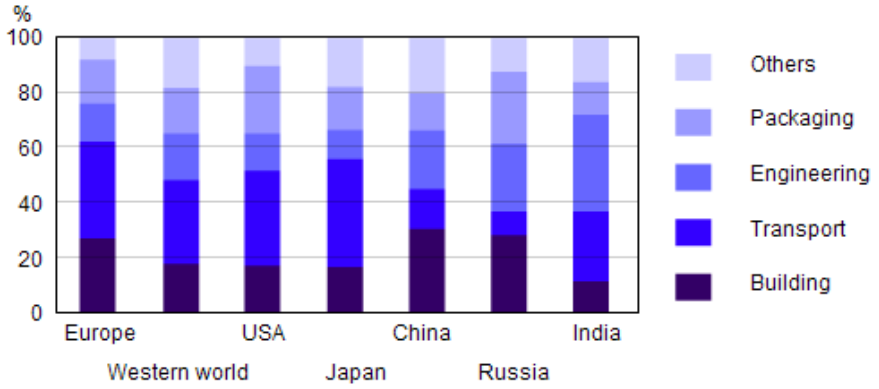

Fig. 2.4: Consumption of aluminium in the world.

In addition aluminium is 100% recyclable. It requires only 5% of the energy needed for the production of the primary metal for the re-melting without downgrading of the quality. Thus it is possible to save large amounts of energy and protect the environment. 42% of cans, 85% of construction materials and 95% of transport vehicles from aluminium will be recycled as secondary aluminium in Europe [Web5].

2.2.2. Aluminium Alloys (AA7075)

Due to the low strength of pure aluminium, most of the commercially used aluminium contains one or more alloying elements such as Zn, Mg, Cu or Si due to which its mechanical properties are remarkably improved. The strength of aluminium alloys depend not only on the components of the specific alloy, but also on the employed heat treatments and manufacturing processes.

Aluminium alloys are divided into two groups, viz. wrought alloys and casting alloys, both of which can be further categorized into heat-treatable (those to be strengthened by heat treatment) and non-heat-treatable (those not to be strengthened by heat treatment) classes.

There are eight series (1xxx to 8xxx) of wrought aluminium alloys where the first digit denotes their main alloying element, e.g. 7xxx series represents aluminium alloys with the highest achievable strength containing Zn as the main alloying element. Fig. 2.5 [Web4] shows the classification of wrought aluminium alloys:

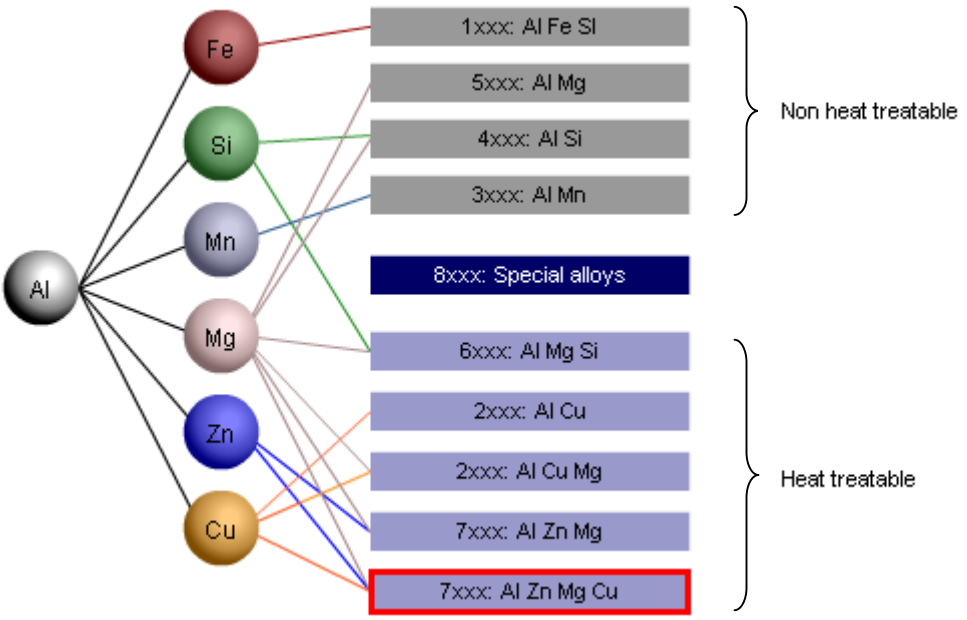

Fig. 2.5: Classification of the wrought aluminium alloy series.

Table 2.2 [Web1] below shows the composition limits of some typical aluminium alloys:

Alloy	Si	Fe	Cu	Mn	Mg	Cr	Zn	Ti
2024	0.50	0.50	3.80-4.90	0.30-0.90	1.20-1.80	0.10	0.25	0.15
5086	0.40	0.50	0.10	0.20-0.70	3.50-4.50	0.05-0.25	0.25	0.15
6061	0.40-0.80	0.70	0.15-0.40	0.15	0.80-1.20	0.04-0.35	0.25	0.15
7075	0.40	0.50	1.20-2.00	0.30	2.10-2.90	0.18-0.28	5.10-6.10	0.20

Table 2.2: Some common wrought aluminium alloys composition in weight percent. The weight concentration of the predominant metal aluminium is not listed explicitly.

Alminium alloys of the 7xxx series of aluminium alloys are widely used as structural material in aerospace and automotive industries because of their high strength and relative low density. Fig. 2.6 shows the application of 7xxx series alloys in the aircraft industry [Wlo07]:

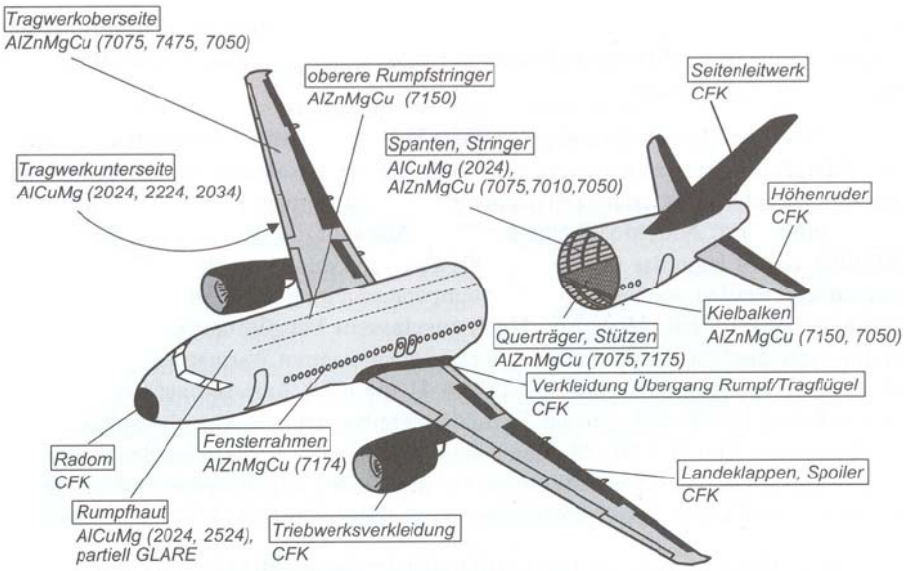

Fig. 2.6: Application of 2xxx and 7xxx series aluminium alloys applied in aerospace industry.

The 7xxx series consists of quaternary Al-Zn-Mg-Cu alloys where Zn is the principal strengthening component. These alloys can be strengthened through precipitation hardening (will be discussed in section 2.3.2 in detail) controlled by Zn and Mg atoms from which the η´ and η phases will be formed as the main hardening mechanism [Buh08]. The hardening potential of Al-Zn alloys is greatly improved by the addition of Mg. Moreover, higher strength and better response to heat treatment compared to binary Al-Zn alloys are achieved. Further addition of Cu (1-2 wt%) as well as small amount of Cr / Mn to the ternary Al-Zn-Mg alloys result in the highest strength aluminium alloys, by which the quench sensitivity and ageing rate is improved [Liv84]. However, as structural materials not only the strength but also the corrosion resistance should be taken into consideration.

In this study an AA7075 alloy is investigated, first developed by a Japanese company in 1936 [Web6]. It contains 5.10-6.10 wt% Zn, 2.10-2.90 wt% Mg, 1.20-2.0 wt% Cu, and less than half a percent of Si, Mn, Ti, and other metals (see Table 2.2). Becaues of its excellent properties AA7075 alloys are extensively applied for the construction of aircraft e.g. airfoil and fuselage. It is also strongly desired in other fields like mould tool manufacture. The mechanical behavior of this alloys is greatly influenced by the temper of the material through which the microstructure can be adjusted. According to the temper procdure the 7075 alloys is categorized into subgroups like 7075-O (Un-heat-treated), 7075-T6 (Solution heat treated and artificially aged) and so on.

2.3. Strengthening Mechanisms

2.3.1. Basics of Strengthening Mechanism

The strength of pure and un-heat-treated aluminium is not sufficient for engineering applications, and different methods have been used to improve not only the strength but also other mechanical properties. The macroscopic deformation of a material originates from the collective movement of dislocations which can be prohibited by strengthening mechanisms such as precipitation hardening, solute hardening, work hardening or grain size hardening.

1) Precipitation Hardening

Precipitation hardening is also referred to age hardening or second phase hardening. Through solid solution heat treatment and quenching a supersaturated solid solution is obtained which tends to transform to the equilibrium structure. But before equilibrium can be achieved some typical phases will be formed that effectively hinder the movement of dislocations. As the most important mechanism in this study it will be described in detail subsequently.

2) Solute Hardening

The illustration of substitutional and interstitial point defects is given in Fig. 2.7 [Web1]. These defects cause lattice distortions and therefore the propagation of dislocations is prohibited by the corresponding stress field. The strengthening depends mainly on the size, the concentration and the electronic configuration of the solute atoms.

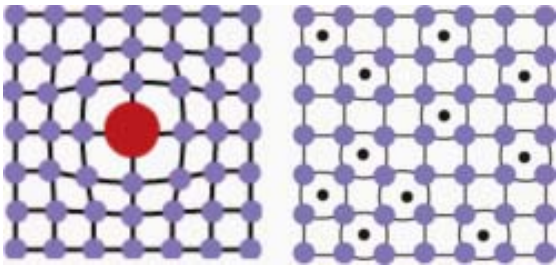

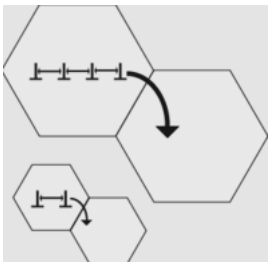

Fig. 2.7 (left): Substitutional/interstitial point defects and the corresponding distortions.
Fig. 2.8 (right): Schematically illustration of pile-up of dislocations at grain boundaries.

3) **Grain Size Hardening**

The mean grain size in a polycrystalline metal affects its mechanical properties. Decreasing the grain size results in a lower number of dislocations per grain, thus under a shear stress the “pressure” built up from pile-up of dislocations at grain boundaries will be reduced, as shown in Fig. 2.8 [Web1] . Thus it is more difficiult for dislocations to move from one grain to another to produce plastic deformation.

4) Work Hardening

Dislocations interact with each other by their corresponding stress fields. By increasing dislocation density through cold-working these repulsive or attractive interactions will be enlarged and as a result a higher shear stress is required for the movements of dislocations. This mechanism can be applied for those alloys, which do no respond to precipitation hardening.

2.3.2. Precipitation Hardening

This section describes how a fine distribution of precipitates can be achieved by suitable heat treatment, which requires an alloy system, in which the solid solubility of one or more alloying elements decreases significantly with lessened temperature. Afterwards the strengthening mechanisms will be explained.

2.3.2.1. Heat Treatment

There are usually three main stages of heat-treatment as illustrated in Fig. 2.9:

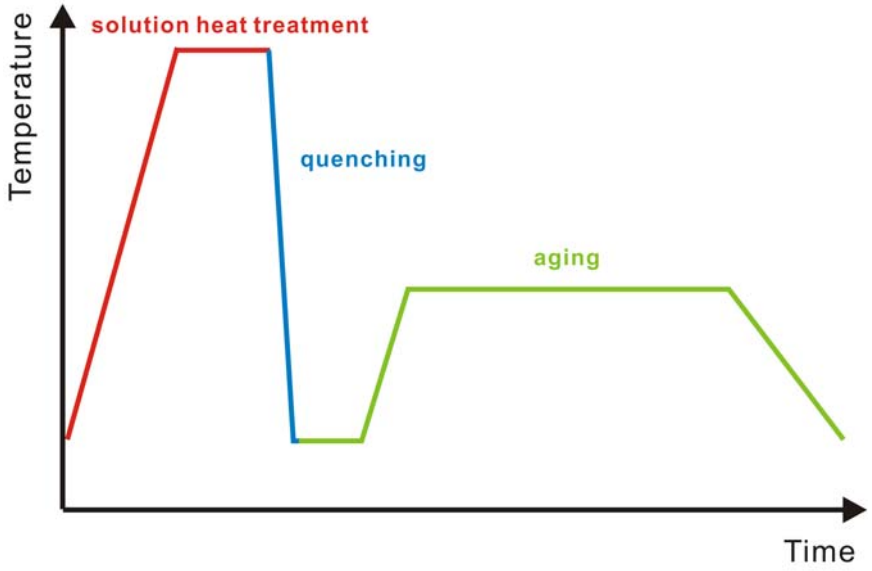

Fig. 2.9: Stages of heat treatment, including heating, quenching and aging successively.

1) Solid solution Heat Treatment

As indicated with the red line in Fig. 2.9, the alloy is heated to an appropriate temperature (e.g. 495° C) and held at this temperature for some time (e.g. 45 minutes) so that all constituents are dissolved in the solid solution. In addition a great amount of thermal vacancies (about 10^{-4} vacancies per atom) are also produced in this stage [Got98].

2) Quenching

The blue quenching line represents rapid cooling of the heated solid solution to a low temperature. Due to the very short cooling time all constituents as well as a considerable fraction of thermal vacancies are "frozen" inside the material effectively. In this case a thermodynamic unstable supersaturated solid solution (SSSS) is produced, since the concentration of solute atoms is higher than the equilibrium level.

3) Aging

The so-called aging process is a relatively low-temperature (green line in Fig. 2.9, even at room temperature) heat treatment, which drives the supersaturated-solid-solution to form a fine distribution of precipitates.

2.3.2.2. Decomposition Processes

The unstable supersaturated solid solution tends to change to the equilibrium state through some typical intermediate stages: e.g. SSSS-GP zones-θ''-θ'-θ for Al-Cu alloys [Zam02].

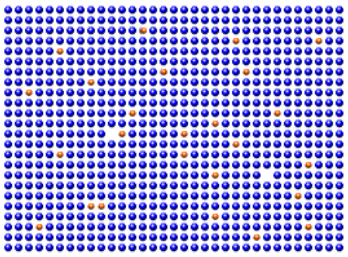

(1) Unstable supersaturated solid solution
is formed after quenching and tends to transform to the equilibrium state. The quenched-in vacancies stimulate the diffusion of solute atoms and the formation of precipitates, indicated in the Fig. 10 as blank. The alloying element B (yellow) is randomly distributed in aluminium matrix A (blue).

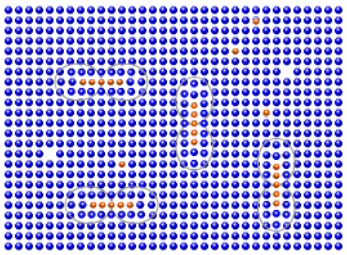

(2) Coherent GP I (Guinier-Preston) zones
are created at the beginning of aging by localization of solute atoms B on specific planes of A lattice. The distortion of the crystal lattice (circle around GP zones) originates from these coherent precipitates, leading to a large increase of the strength.

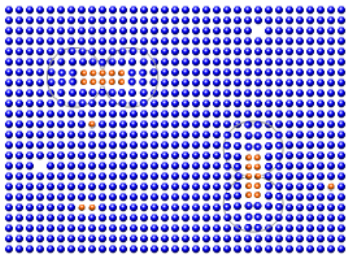

(3) Quasi-coherent intermediate phase (e.g. θ'' phase)
is also regarded as GP II zones. Such a quasi-coherent intermediate phase is formed on the basis of GP I zones. Thus their size is larger. In this case the strengthening of alloys is maximized due to the increment of coherency strain (larger distortion).

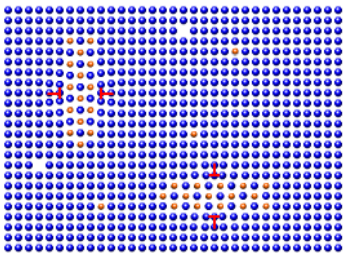

(4) Semi-coherent intermediate phase (e.g. θ' phase)
in the case of aging, the coherent phase turns into semi-coherent phase of even larger size as a result of the formation of dislocations at the interface. Not only the coherency strain but also the strength of the alloys is thus reduced as a consequence.

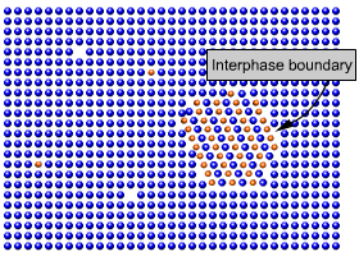

(5) Incoherent equilibrium phase (e.g. θ phase)
The incoherent equilibrium phase is finally achieved upon sufficient aging time / temperature with a different crystal structure separated from aluminium matrix by the new interphase boundary. The elimination of coherency strain leads to further reduction of the strength.

Fig. 2.10: A schematic example of the decomposition process of Al-Cu binary alloy system, in which different precipitates are formed in sequence [Web4].

The following micrographs show typical GP zones, θ' and θ precipitates in an Al-Cu alloy aged under different conditions as an example:

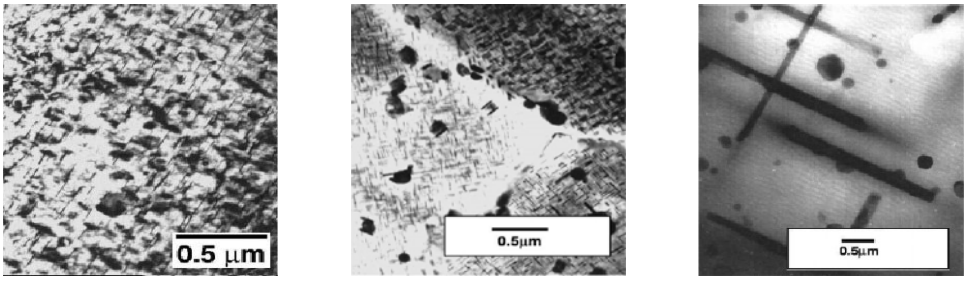

(a) (b) (c)

Fig. 2.11: Micrographs of precipitates in Al-Cu, shows Cu rich GP zones obtained by aging for 6 hours at 180°C, θ' precipitates aged for 2 hours at 200°C and θ precipitates with aging time of 45 minutes at 450°C in Al-4%Cu alloys [Jac].

Alloys based on Al-Zn-Mg-Cu system such as AA7075 investigated in this study exhibit the following precipitation sequence [Buh08]:

$$SSSS \rightarrow GP\ zone \rightarrow \eta' \rightarrow \eta(MgZn_2)$$

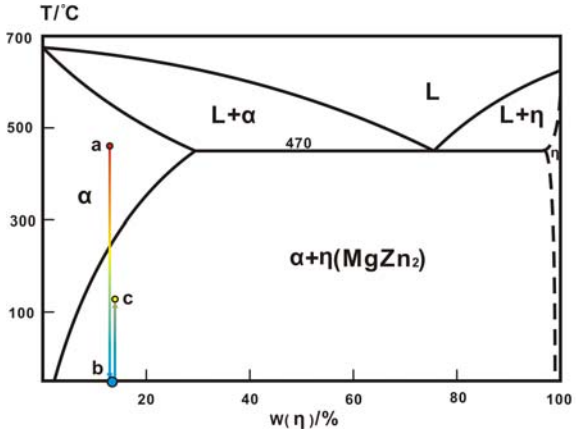

Fig. 2.12: Phase diagram of Al-Zn-Mg alloys

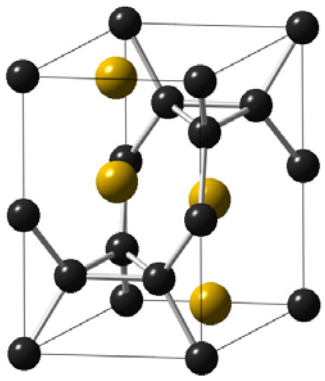

Fig. 2.13: Crystal structure of η

After solid solution heat treatment and quenching, the alloy is heated up from room temperature to a relative low aging temperature so that fine dispersion of GP zones of roughly spherical shape (diameter 2-3nm) is produced. Not only the size of the GP zones but also the strength of the alloy increase with aging time (e.g. at 177°C the diameter is about 6nm).

Further aging leads to the formation of the partially coherent intermediate η′ precipitate (which is generally believed to be responsible for the highest strengthening, [Buh08]), as the precursor of the equilibrium phase η ($MgZn_2$, crystal structure is shown in Fig. 2.13). Other types of precipitate such as T′ / T will be formed which depend on the amount and ratio of Mg and Zn [Now07]. Both of η′ and η phase are of hexagonal structure as illustrated by Fig. 2.13 [Fri26,Web7]. The complete process is shown in the Fig. 2.12 from a to c via b.

2.3.2.3. Strengthening Processes

The precipitation process was described in the previous section and the actual strengthening processes, by which the mobility of dislocations is limited, are explained in the following. There are mainly three kinds of strengthening mechanisms in the case of precipitation hardening:

- dislocation movement prohibited by strain fields (coherency strain hardening).
- dislocations cutting through particles (chemical hardening).
- dislocations bowing around particles (dispersion / precipitation hardening).

1) Dislocation movement prohibited by strain field

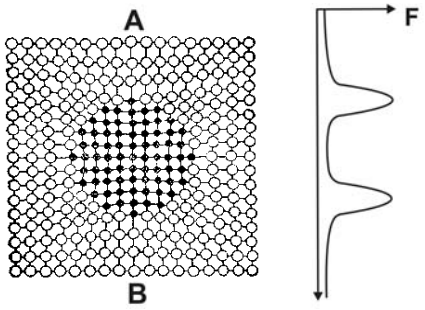

Fig. 2.14: Lattice distortion caused by coherent GP Zones, larger shear stress is required for dislocations to move form position A to position B due to corresponding strain field.

In this case larger GP zones are formed in the early stages of the precipitation sequence by aging of the SSSS, as discussed before. Taking alloy system like Al-Cu as an example, the coherent structure of GP zones results in a high strain field in the surrounding region, as illustrated in Fig. 2.14. As a result larger force is required for the movement of dislocations from A to B through the GP zone. In this way the alloy is strengthened.

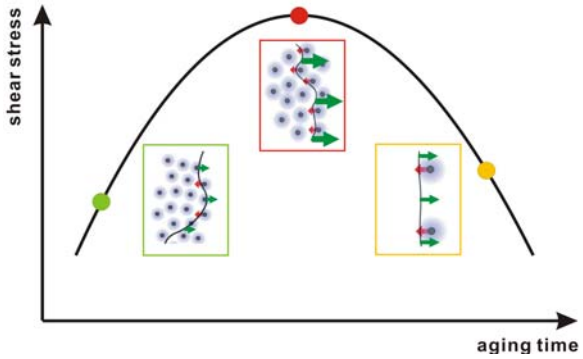

Fig. 2.15: Dependency of shear stress on size, spacing and strain fields of precipitates. Shear stress (green arrows) required to over the resistance (red arrows) due to corresponding strain field (gray area surrounding precipitates) is schematically illustrated.

At the beginning GP zones are small but by longer aging time the precipitates will be separated more widely from each other, each having a larger size and a larger corresponding strain field as well. The coherency strain hardening will be maximized when the average zone spacing roughly equals the curvature radius of dislocation [Web4].

2) Dislocations cutting through particles

Dislocation can cut a coherent particle (a zone or precipitate) [Cla05]. The stress required depends on the stress field of the particle and on the extra energy, which is required to create the new interfacial areas.

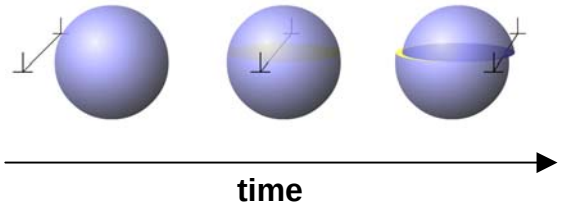

Fig. 2.16: Dislocations cutting through a particle. Yellow surface indicate the new interfacial area.

The critical stress σ depends on the radius of the zone / precipitate r as:

$$\sigma \propto \sqrt{r} \tag{2.1}$$

There it can be concluded that the material strength increases with increasing radius since it is more difficult for dislocations to cut through large particles.

3) Dislocations bowing around particles

Incoherent precipitates will be formed with sufficient long aging time or higher temperature. In this situation it is no longer possible for dislocations to cut through these precipates due to their incoherent structure. Therefore dislocations pass incoherent precipitates by different mechanisms, one of the most important is known as the Orowan bowing, as illustrated in Fig. 2.17:

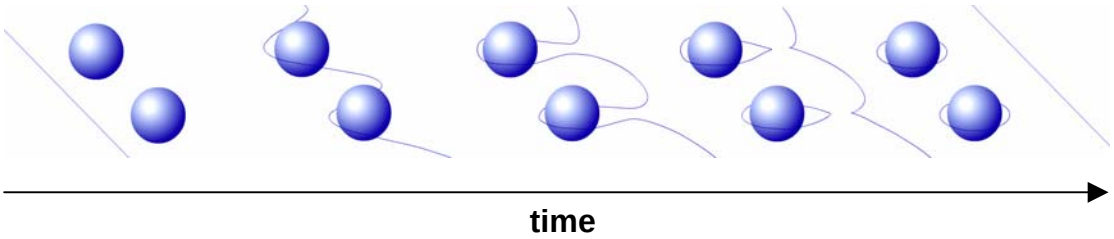

Fig. 2.17: Orowan bowing process. Dislocation (blue line) bowing around incoherent precipitates (blue spheres), after which dislocation loops are left.

In this case the functional dependency of the critical stress is:

$$\sigma \propto \frac{1}{r} \tag{2.2}$$

Now the strength is anti-proportional to the radius which means that dislocations are more likely to bowing around particles of larger size. In addition dislocation loops around particles are left when they pass by and this will lead to work hardening afterwards due to interactions with subsequently passing dislocations [Web4].

According to the governing equations above, the radius of the precipitate particles determines whether dislocations cut through or bow around particles. The optimal radius to achieve the maximal strengthening is then [Haa84]:

$$r_{optimal} = \sqrt[3]{3} \cdot \frac{G \cdot b^2}{\gamma} \tag{2.3}$$

where G is the shear modulus, b is the magnitude of the Burgers vector and γ is the surface energy. Fig. 2.18 schematically shows $r_{optimal}$ obtained under the consideration of both mechanisms:

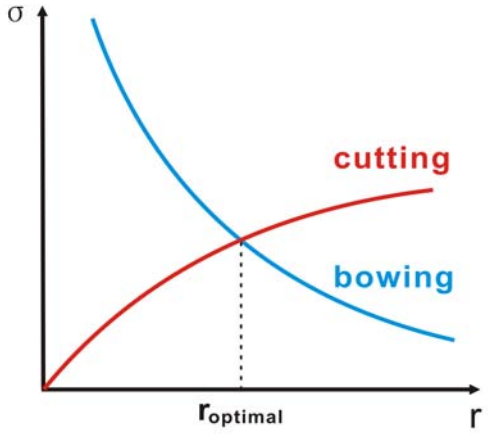

Fig. 2.18: Optimal radius for strengthening. The maximal strengthening is achieved with the optimal radius, where the critical stress from both mechanisms equals.

Fig. 2.19 shows the combined aging curve (black), obtained by considering 4 strengthening mechanisms, namely coherency strain hardening, solute hardening, chemical hardening and dispersion hardening (curve 1-4). It should be noticed that many alloys make use of them altogether.

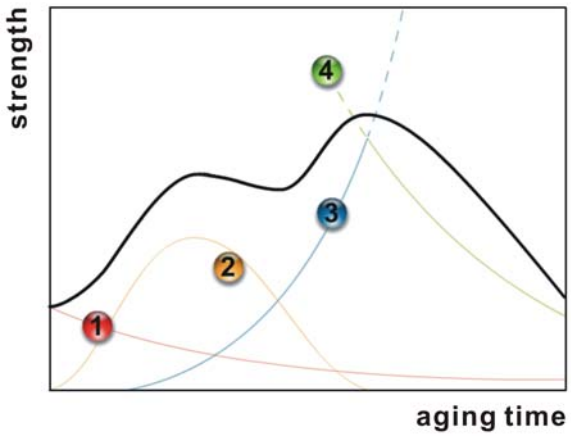

Fig. 2.19: The combined aging curve based on 4 different strengthening mechanisms [Web4].

For short, the maximum strengthening of alloys can be achieved at certain aging time. Excessive aging leads to decreases of the strengthening effect as a result of the larger size and incoherent structure of the produced precipitates.

2.4. Positron Annihilation Spectroscopy

2.4.1. Discovery of Positrons and Its Applications

The positron is the antiparticle of the electron. It has the same mass as an electron, its spin is 1/2, but it has an electric charge of +e. It annihilates with an electron, which predominantly results in the emmision of two γ quanta of 511keV. In 1928 Paul Dirac predicted the existence of positrons theoretically as a consequence of his famous Dirac equation. Two years later the Chinese physicist Chung-Yao Chao detected an anomalous absorption of high energetic γ rays in lead, in which positrons were involved, but unfortunately without further identifications [Meh00]. Finally, the American physicist C. D. Anderson discovered positrons in a cloud chamber in 1932 [And33] which is shown in Fig. 2.20:

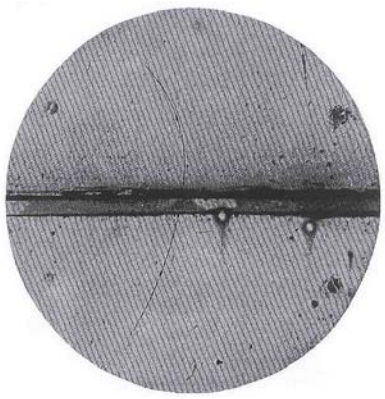

Fig. 2.20: Cloud chamber photograph of the first identified positron from C.D. Anderson.

Since then, lots of research was carried out using positrons produced by cosmic rays or nuclear reactions. The discovery of the positron motivated physicists to reconsider about elementary particles, matter and antimatter, which contributed to the development of physics and philosophy enormously.

Positron Annihilation Spectroscopy (PAS) is a nuclear technique which is used in solid state physics, material science, chemistry etc. After a positron has entered a solid, it will annihilate with electrons and 511keV γ quanta will be released as consequence. These quanta can be detected by different methods like Positron Lifetime Spectroscopy (PLS), Doppler Broadening Annihilation Radiation spectroscopy (DBAR) and Angular Correlation Spectroscopy (ACS) accordingly. The spectroscopic signals, which depend on defects and phase transitions, give useful information about the microstructure in solids. Compared to other experimental techniques, PAS has some great advantages: it is non-destructive, there are almost no limits about the sample geometry, measurement under broad temperature ranges is possible and it is uniquely sensitive to open volume defects like atomic sized vacancies.

2.4.2. Positron Sources

There are two ways to produce positrons:

1) e^+e^- pair production utilizing Bremsstrahlung.
2) Different isotopes such as ^{22}Na or ^{68}Ge are widely used due to their simplicity, as shown in Fig. 2.21 [Klo07]:

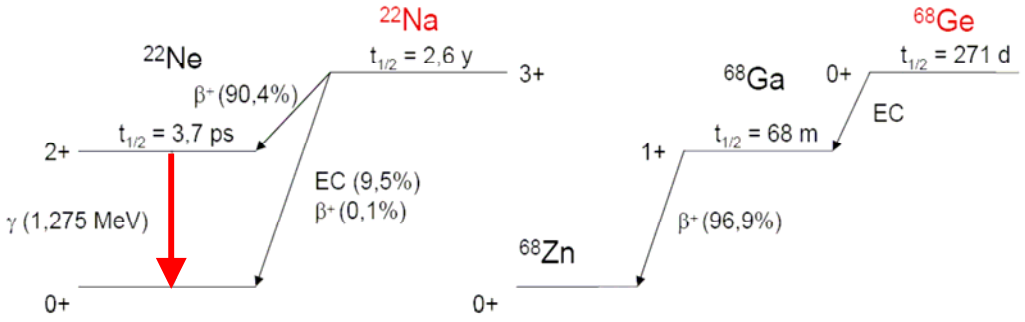

Fig. 2.21: Decay diagram of ^{22}Na and ^{68}Ge.

^{22}Na is the most widely used positron source in laboratories due to its relatively long half-life time. Usually it is delivered in the form of NaCl, which is capsuled e.g. by a thin aluminium foil. This protects the source from being damaged but on the other hand part of the positrons will annihilate in these foil, thus a source correction may be required. The excited state of $^{22}Ne^*$ is reached by β^+ decay and then the ground state is reached by emitting a 1.275MeV γ quantum in about 3ps, which is almost a simultaneous emission as the positron. This feature enables ^{22}Na to be an ideal source for positron lifetime measurements, in which the 1.275MeV γ quantum is used as the start signal of the logic circuit and the annihilation γ as the stop signal afterwards. But on the other hand this gamma causes Compton background in energy spectra that can not be neglected. This leads to a bad signal/noise ratio and an accurate calculation of the background is not possible. Therefore other sources may have to be used for energy resolving methods such as Doppler broadening annihilation radiation spectroscopy.

In such a case it is better to use ^{68}Ge as a source for the DBAR method due to its significant lower background in the photo peak, which enables the analysis of the high momentum part of the annihilation radiation even with a single Ge detector. As shown in Fig. 2.21, ^{68}Ge decays into ^{68}Ga by electron capture and then 97% from that decays into ^{68}Zn by β^+ decay, the other 3% of ^{68}Ga produce a γ line of 1.077MeV, which can actually be neglected. In this study we produced the ^{68}Ge source via a (d, 3n) nuclear reaction. Deuterons are accelerated to 27 MeV with the cyclotron at the Helmholtz-Institut für Strahlen- und Kernphysik and directed on the target which is made from the commercially available semiconductor wafer GaP with a thickness of about 100 µm in order to avoid too much positron annihilation in itself. Metallic Ga can not be used as the target material due to its low melting point. After the irradiation a “clean” ^{68}Ge source is produced. “Clean” here means that ^{68}Ge is stable inside the wafer. Other undesired isotopes like ^{69}Ge are also produced through (d, 2n) reaction but will vanish in some weeks due to its short half-life.

2.4.3. Positrons Trapping and Annihilation in Solid

Positrons produced by β^+ decay usually have kinetic energies ranging from keV to MeV. By Bremsstrahlung and phonon scattering etc. positrons are thermalized rapidly within few picoseconds. For positrons from ^{22}Na this results in a reduction of kinetic energy from hundreds of keV to about 40meV (room temperature) within 1-3ps. After the thermal energy is reached, positrons begin to diffuse and occupy a delocalized state. Due to their positive charge they are repelled by the nuclei, thus the maximum probability density of position is localized in the interstitial region. Positrons are trapped very easily by lattice defects like vacancies, which have an attractive potential originating from absence of nuclei, as shown in Fig. 2.22 [Kra99]:

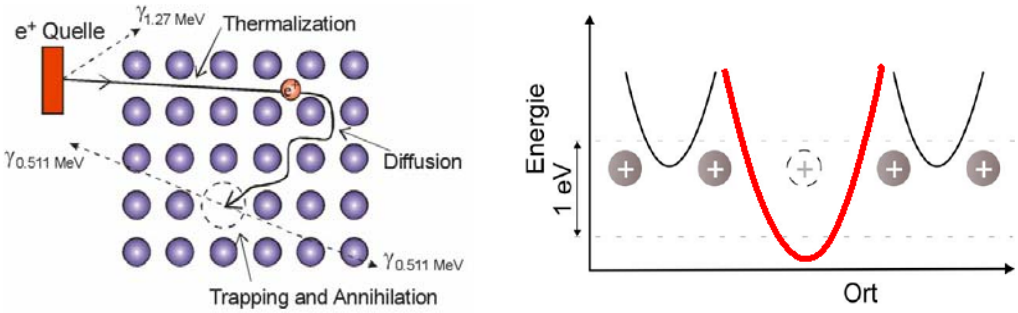

Fig. 2.22: (a) Annihilation of the trapped positron after thermalization and diffusion. (b) The attractive potential (red part) of vacancy due to absence of nuclei.

Precipitates and their corresponding interfaces can also be the places of positron trapping. Fig. 2.23 shows the potential and positron wave functions for coherent precipitates e.g. GP zones, coherent precipitates with vacancy and semi-coherent/incoherent precipitates, respectively. The probability of positron trapping is very high for vacancies and interface regions due to misfit defects.

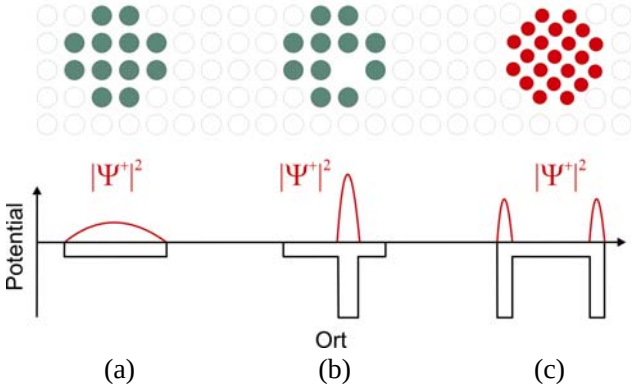

Fig. 2.23: Potential and wave function of positrons of different types of precipitates. (a) fully coherent, (b) fully coherent with vacancy, (c) semi-coherent/incoherent precipitates [Klo07].

The trapping rate κ_d of positron into defects is proportional to the defect concentration C_d: $\kappa_d = \mu C_d$, where μ is the trapping coefficient. Besides the dominating trapping process positrons have also the possibility of de-trapping but normally this process can be neglected.

2.4.4. Basics of Positron Annihilation Techniques

Positrons trapped by crystal defects annihilate with electrons into 2γ quanta of 0.511MeV by mass-energy transformation (3γ process is also possible but very infrequently, the ratio between 2γ and 3γ events is about 371:1). Annihilation parameters contain information about the defect type, the concentration of the localization site and its chemical environment originating from different electron densities and electron momentum distribution between the defect-rich and the defect-free crystal.

Positron annihilation techniques are categorized into 2 fundamental groups, viz. PLS and DBAR techniques as shown in Fig. 2.24 [Bon]. Other techniques like angular correlation spectroscopy are not relevant for this work, therefore will not be discussed.

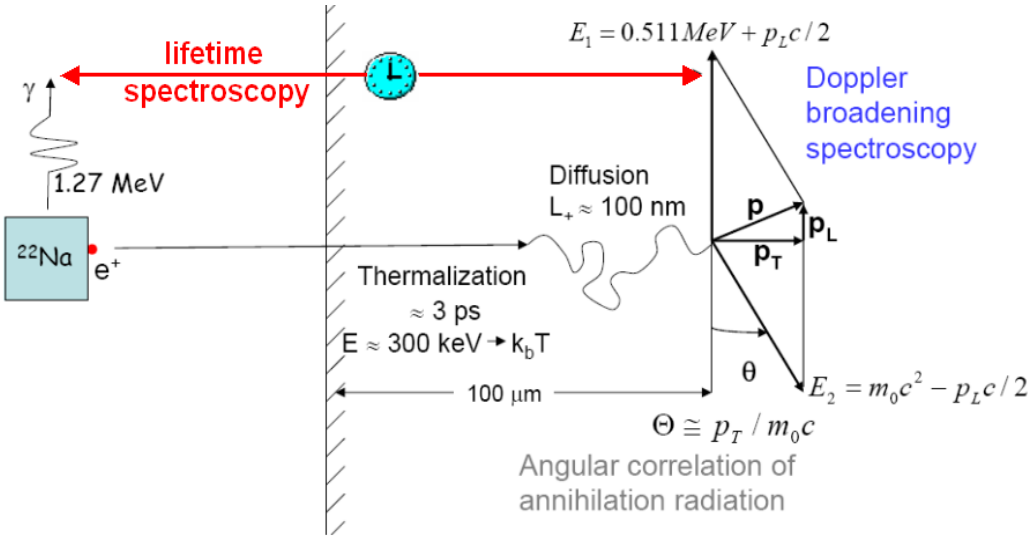

Fig. 2.24: Principles of positron lifetime spectroscopy (red part) and Doppler broadening annihilation radiation spectroscopy (blue part).

(1) **Positron lifetime spectroscopy**

Positron lifetime spectroscopy utilizes the dependence of positron lifetime on electron density and is measured as the time difference between the 1.27MeV γ quantum simultaneously generated with the "birth" of the positron and one of the 0.511MeV annihilation γ quanta afterwards, which is illustrated with the red part of Fig. 2.24. Different defect components can be measured and distinguished by their corresponding lifetimes.

(2) **Doppler broadening annihilation radiation spectroscopy**

If the initial overall momentum of the annihilating e^+ - e^- pair is zero then the 2 annihilation γ quanta will propagate in the opposite direction with the energy of 0.511MeV. But this is actually not the case due to the momentum of the electron and due to the fact that the momentum of the positron can be neglected. According to energy and momentum conservation this leads to an angle θ as well as a Doppler shift ($\pm p_L c/2$) at the annihilation energy of the propagation direction, as illustrated in Fig. 2.24. A symmetric distribution of the Doppler broadened spectrum centered at 0.511MeV is added up after millions of annihilation events. The shape of the energy peak can be analyzed to obtain information about the electron momentum distribution.

2.4.4.1. Positron Lifetime Spectroscopy

Generally the positron lifetime is measured as the time difference between the birth γ quantum (1.27MeV, start signal) and one of the annihilation γ quanta (0.511MeV, stop signal) in the sample. The positron lifetime τ is the reciprocal of the annihilation rate λ which is a function of the positron and electron density $n_{\pm}(r)$ at the annihilation site:

$$\tau = 1/\lambda \qquad \lambda \propto \int n_{+}(r) n_{-}(r) \gamma dr \tag{2.4}$$

where **r** is the real space vector and γ is a function on account of the e^{+} - e^{-} coulomb interaction [Kra99]. Typical values of positron lifetime in defect-free metals vary between 100-250ps and increase in the presence of defects due to the locally reduced electron density.

(1) Trapping model

The simplest trapping model schematically illustrated in Fig. 2.25 can be used to demonstrate positron trapping in a single open volume defect type like vacancies. There are two possibilities of positron annihilation after thermalization: (1) annihilation in defect-free bulk with the annihilation rate λ_b, (2) trapping in vacancy with the trapping rate κ_d and annihilation with smaller annihilation rate λ_d. It should be noticed that thermal de-trapping from vacancy is excluded.

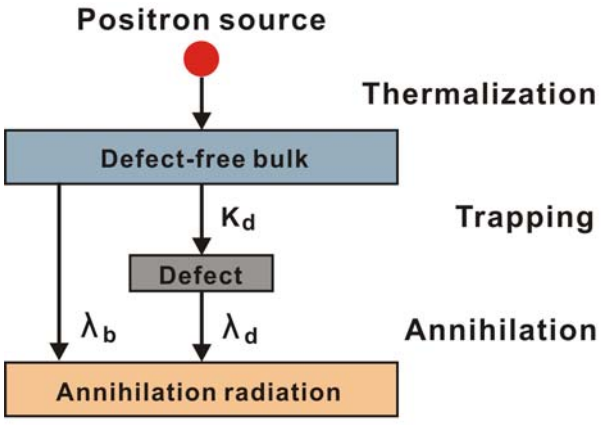

Fig. 2.25: Illustration of trapping model with one defect type.

This model can be described by rate equations whose solution is:

$$D(t) = I_1 \exp(-\frac{t}{\tau_1}) + I_2 \exp(-\frac{t}{\tau_2}) \tag{2.5}$$

with the following abbreviations:

$$\tau_1 = \frac{1}{\lambda_b + \kappa_d}, \qquad \tau_2 = \frac{1}{\lambda_d}, \qquad I_1 = 1 - I_2, \qquad I_2 = \frac{\kappa_d}{\lambda_b - \lambda_d + \kappa_d} \tag{2.6}$$

where τ_1 is the reduced bulk lifetime, τ_2 equals to τ_d since de-trapping is neglected and the intensities I_i correspond to lifetime components τ_i. These parameters can be obtained by a non-linear fit of the measured spectrum after background subtraction and source correction [Kra99].

The trapping rate can be calculated as:

$$\kappa_d = \mu C = I_2\left(\frac{1}{\tau_1} - \frac{1}{\tau_2}\right) = \frac{I_2}{I_1}\left(\frac{1}{\tau_b} - \frac{1}{\tau_d}\right) \tag{2.7}$$

where C is defect concentration and μ is the specific trapping rate, which depend on temperature and characteristics of the defect type [Haa03]. The fraction of trapped positrons is:

$$\eta = \int_0^\infty n_d(t)dt = \frac{\kappa_d}{\lambda_b + \kappa_d} \tag{2.8}$$

where $n_d(t)$ is the number of positrons in the defect at time t [Kra99].

(2) Positron lifetime spectrum

The positron lifetime spectrum is a statistical distribution of positron lifetimes through random annihilation events, as shown in Fig. 2.26. Its functional behavior is an exponential decay (red curve) and becomes a superposition of exponential decays corresponding to different lifetime components (blue curve).

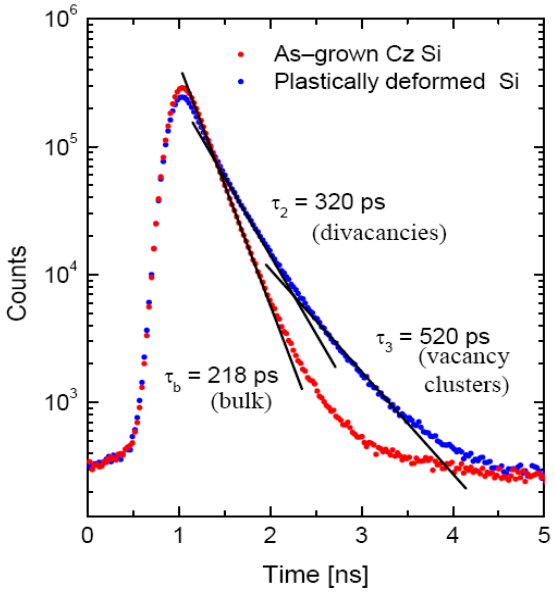

Fig. 2.26: Positron lifetime spectrum from as-grown and plastically deformed silicon. Spectrum corresponding to defect-rich silicon is located above the defect-free silicon, which originates from the different long life components like τ_2 and τ_3 [Kra99].

Information about the size of the free volume associated with different defect types and the intensity related defect concentration can be obtained after the data analysis.

2.4.4.2. Doppler Broadening Annihilation Radiation Spectroscopy

The Doppler broadening spectroscopy has been proved to be a very useful tool for the study of defects in materials like Aluminium-alloys in the past years. It makes use of the momentum conservation of the e^+ - e^- pair during the annihilation process, from which information about the electron momentum distribution of the sample material can be extracted afterwards.

The momentum of the e^+ - e^- pair is transferred to the annihilation γ quanta. The component p_L in the propagation direction is a variable randomly distributed around zero which results in an energy shift ($\Delta E = \pm p_L c / 2$) by the 0.511MeV annihilation peak, and after sufficient events a symmetrical broadening of the annihilation peak can be obtained.

1) Line Shape Parameters

A Doppler broadening spectrum contains two major parts: the low momentum part corresponding to valence electrons and the high momentum part corresponding to core electrons, respectively. For the quantitative evaluation two line parameters are defined. The Shape parameter S is the central low momentum part A_s (yellow) divided by the total area A_0 below the curve and the Wing parameter W is defined as the ratio between the high momentum interval A_w (green) to A_0 as indicated in Fig. 2.27 [Kra99]:

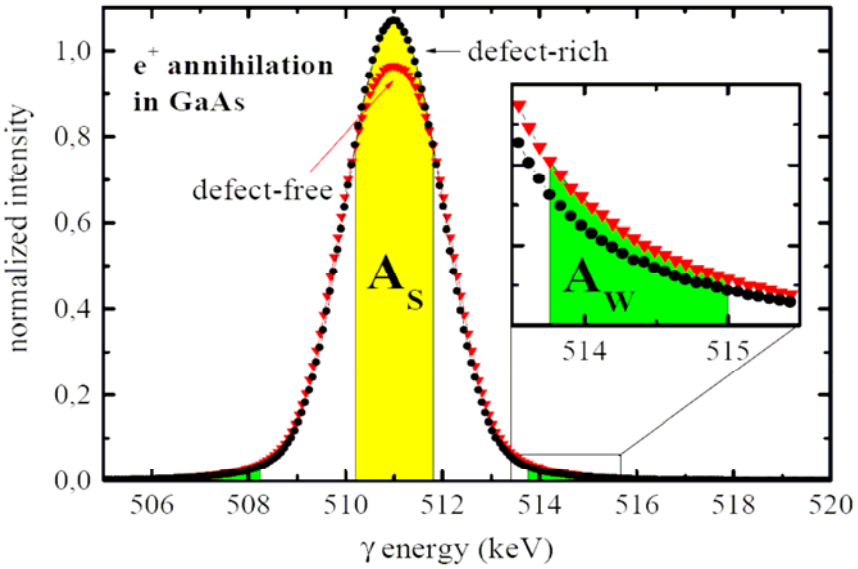

Fig. 2.27: Dependence of Line Shape Parameters on defect

$$S = \frac{A_s}{A_0}, \quad W = \frac{A_w}{A_0} \tag{2.9}$$

For those positrons trapped by open volume defects the Doppler broadening spectrum will become higher and narrower since the probability of positron annihilation with low momentum valence electrons is significantly increased compared to the annihilation with high momentum core electrons. Fig. 2.27 reveals the dependence of the line shape on defect concentration in the material. This effect can be used for the investigation of these defects.

2) High momentum analysis (HMA)

The so-called high momentum analysis can be used for the determination of the chemical surroundings at the annihilation site. By mirroring the low energy side of the spectrum to the high energy side, the sum of both can be plotted. Fig. 2.28 (a) shows Doppler spectra of well annealed pure Al and Cu normalized to the same area as an example. The ratio plot can be obtained then by normalization of the Cu curve to a well annealed aluminium curve. In this way the element specific differences can be evaluated, e.g. the ratio-plots of annealed Cu and quenched AA2024 are given in Fig. 2.28 (b):

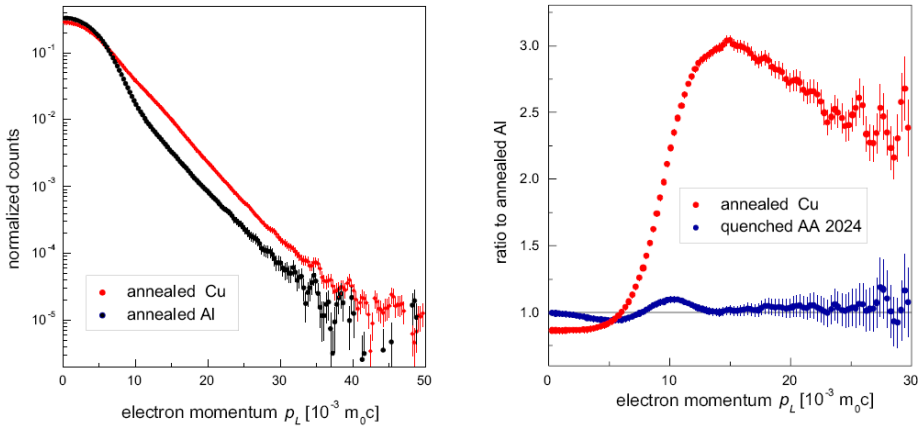

(a) (b)

Fig. 2.28: (a) Doppler spectra of well annealed Pure Al and Cu after high momentum analysis. (b) Ratio-plot of annealed Cu and quenched AA2024 [Haa06].

The difference between Al and Cu originates from the electrons of the 3d-orbital from cu. The electronic configuration of Al is [Ne] 3s2 3p1 and for Cu is [Ar] 3d10 4s1. Therefore such a fingerprint indicates the presence of Cu in an alloy.

Nevertheless, the term “HMA” itself refers to a sophisticated method of background subtraction, which is employed in the case of a single Ge-detector. The details of this method are described in section 3.3. All DBAR results presented in this work were obtained using this method.

2.5. X- ray Absorption Spectroscopy

2.5.1. Basics of X-ray Absorption Spectroscopy

The XAS technique measures the energy dependence of the x-ray absorption coefficient μ(E) on energy. Once x-rays are absorbed by an atom due to the photo-electric effect, the excited core electron will be ejected and a core hole is produced, which will be refilled by another electron from a higher energy level. The energy of the transition between two energy levels will be released in the form of characteristic fluorescence radiation or Auger electron, which is illustrated in Fig. 2.29 [New08]:

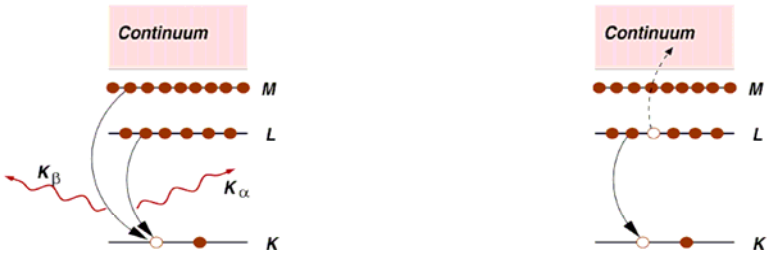

Fig. 2.29: Illustration of characteristic fluorescence radiation (left) and Auger electron (right).

The intensity of the x-ray beam will decrease from I_0 to I due to absorption in a material of thickness t which can be described by Lambert Beer equation $I = I_0 \exp(-\mu t)$. The energy dependence of μ can be measured in two ways, namely by measuring the transmitted x-ray intensity I_t or the intensity I_f of the emitted fluorescence. The schematic description of these methods is shown below:

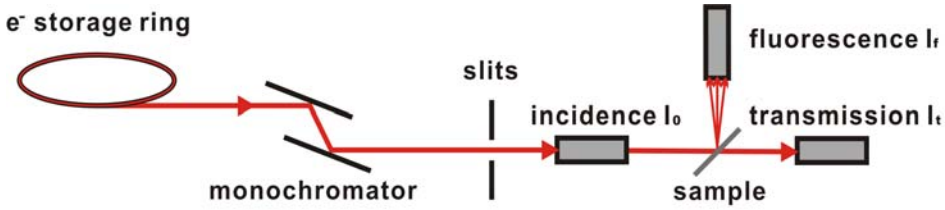

Fig. 2.30: Schematic diagram of the measurement of absorption coefficient.

A white x-ray beam is generated from the electron storage ring and its energy is selected by a monochromator consisting of two parallel crystals which can be turned simultaneously. Only the x-rays with energies that satisfy Bragg's law $n\lambda = 2d\sin(\theta)$ are diffracted. Thus the monochromatic beam propagates through slits by which the beam profile can be defined in both horizontal and vertical direction. The incident beam is transmitted and scattered by the sample. Three ionization or scintillation detectors are required for the measurement of the intensity of the incident, transmitted beam and fluorescence respectively. The fluorescence detector is placed perpendicularly to the incident beam to obtain the best signal/background ratio since the intensity of the scattered x-rays is minimum at the angle 90°. In this way the absorption coefficient is calculated by the following equation:

$$\mu(E) \propto I_f / I_0 \text{ (fluorescence mode)}, \qquad \mu(E) = -\frac{\ln(I/I_0)}{t} \text{ (transmission mode)} \qquad (2.10)$$

2.5.2. XANES and EXAFS

The absorption coefficient μ(E) increases sharply if the energy of the x-rays equals the energy required to excite a core electron to the continuum, which is the so-called absorption edge in the spectrum. Above the edge μ(E) is a smooth function in case of a single atom (blue curve in Fig. 2.31) or it oscillates (red curve in Fig. 2.31) as a result of the interference of the photo-electrons with themselves due to scattering from neighboring atoms.

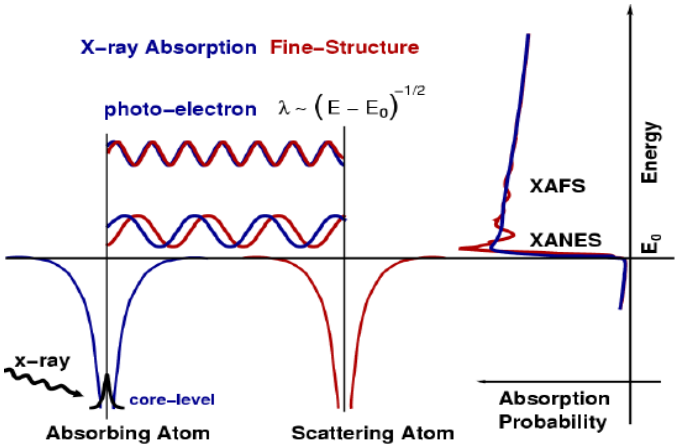

Fig. 2.31: Schematic diagram of the sharp absorption edge and oscillation structure [New08].

Usually a full XAS spectrum is measured from 100eV below the absorption edge to about 1000eV above the edge. It is categorized into two groups according to the energy range considered, namely X-ray Absorption Near Edge Spectroscopy (XANES) and Extended X-ray Absorption Fine Structure (EXAFS), which are located near and above the absorption edge correspondingly, as shown in Fig. 2.32 [New08]:

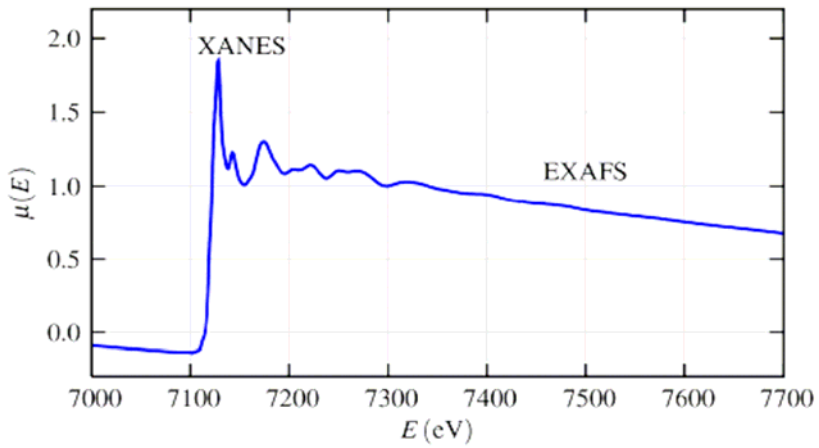

Fig. 2.32: XANES and EXAFS.

For this study XANES spectra were taken at the K edge (9659eV) of the main alloying element Zn. The measured spectra are processed with the software package Athena [Web8] and compared to FEFF calculation [Web9] results afterwards.

Chapter 3
Experimental Procedure

3.1. Sample Preparation

The samples were prepared by cutting different sample materials into pieces with a surface area of about 10mm x 10mm and a thickness of about 1-3mm, depending on the sample material and the applied sources. This ensures that as many positrons as possible annihilate in the sample material rather than in the surroundings. In order to avoid disturbances originating from an oxidation layer, contaminations etc, the surfaces of the samples were sufficiently smooth and clean. This could be achieved by mechanical grinding with successively employment of sandpapers from class 800 to 2400. After grinding the samples were put into a glass with ethyl alcohol inside and were then cleaned in an ultrasonic bad. The heat treatment of the sample is in the next step.

3.1.1. Pure Al Samples for DBAR Measurements

All samples for this measurement are prepared from an aluminium rod (diameter 9.68mm, purity 99.999%) of the company Alfa Aesar GmbH&Co KG. All aluminium references used for DBAR were annealed in vacuum at 620° C for 3 hours. An overview of the samples for quenched-in vacancy measurements is listed in table 3.1:

Sample	Thickness	Heating	Housing	Quenching method
Al_AQ_RT	3mm	475° C, 45 minutes	no	water at room temperature
Al_AQ_HCl1	3mm	495° C, 45 minutes	no	HCl solution at -70° C
Al_AQ_HCl2	1.5mm	495° C, 45 minutes	yes	HCl solution at -70° C

Table 3.1: Overview of pure aluminium samples used for quenched-in vacancy experiments.

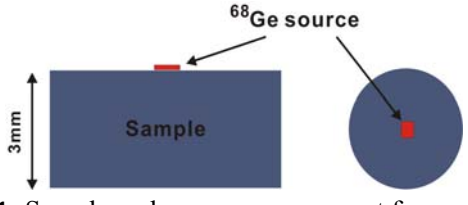

Fig. 3.1: Sample and source arrangement for sample 1.

(1) The first sample was prepared in a relatively simple way: sample 1 was heated at 475° C for 45 minutes and quenched in water at room temperature. The ^{68}Ge source was placed in the middle of the sample surface, as shown in Fig. 3.1. All together it took about 4.5 minutes for evacuation of the system and cooling of the sample stage before the measurement began.

(2) Sample 2 consists two pieces of aluminium plates, both of which are 3mm thick. They were heated at 495° C for 45 minutes, but subsequently quenched in a HCl solution at -70° C instead. After quenching sample plates were cleaned and dried by using cold paper soaked with ethyl alcohol to remove the acid. This quenched sample was stored in liquid nitrogen afterwards and this process was repeated for all sample plates. Then they were assembled in sandwich geometry (blue part in Fig. 3.2) inside liquid nitrogen to avoid loss of vacancies before measurement starts. The reason for applying the second plate from the top is due to the consideration of the ice layer very likely to be formed on the upper surface of sample plate 2, which has considerable influence on the measurement result consequently.

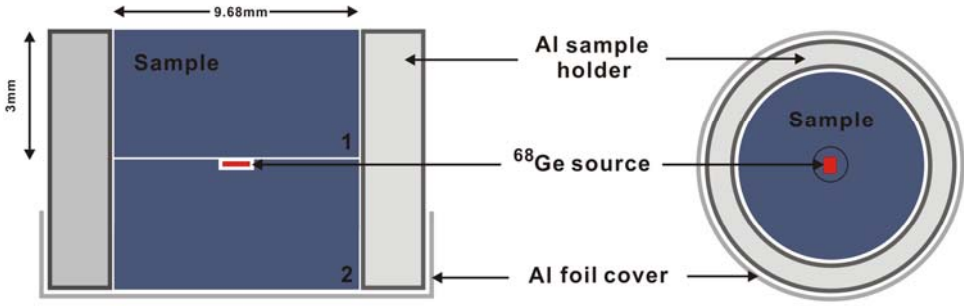

Fig. 3.2: Sample and source arrangement for sample 2.

However it is difficult to realize such arrangement in liquid nitrogen since sample plates could probably be moved against each other accidentally. By using an Al sample holder this problem was solved. The holder was covered with thin Al foil from the bottom for easier disassembly after the measurement. Another difference compared to sample 1 is the concavity manufactured for sample plate 2, this has two advantages: (1) protect the source from being crushed due to the sample above, (2) it is easier to place the source at the right position, especially useful by the presence of weltering liquid nitrogen. When this was done, the system was evacuated and cooled to -70° C without sample. By stop pumping and de-evacuating, cold air inside a liquid nitrogen container was transported into the vessel due to the low pressure. Then the vessel was opened quickly in order to mount the sample on the stage under temperature control. All these attempts enable us to maintain as much vacancies as possible inside the sample material.

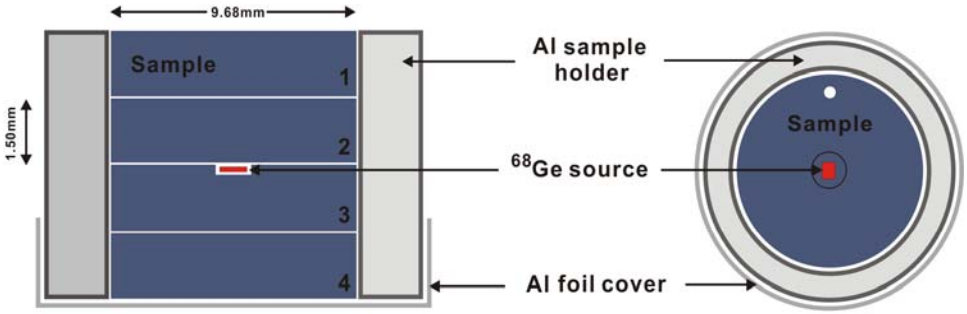

Fig. 3.3: Sample and source arrangement for sample 3.

(3) Sample 3 includes four pieces of plates, each of which is 1.5mm (see Fig. 3.3). They were heated and quenched with further optimized techniques (see next page). Other treatments were the same as for sample 2.

After solid solution heat treatment most of the samples were quenched in water at room temperature, but in order to increase the quenching rate and freeze vacancies directly after quenching an optimized setup was applied [Len76], as shown in Fig. 3.4:

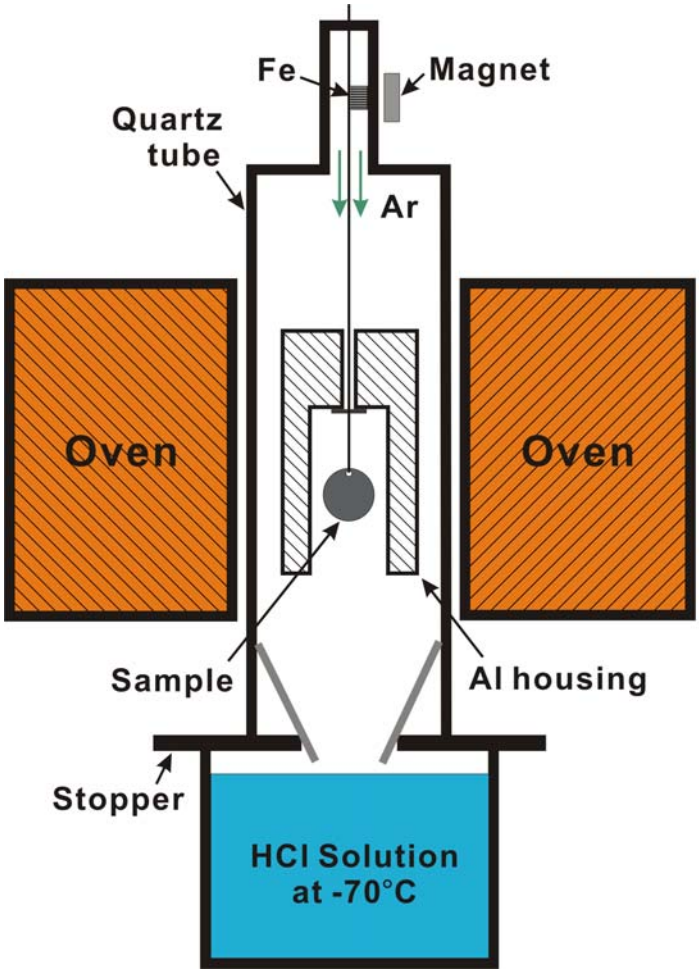

Fig. 3.4: Illustration of the optimized quenching setup. Details will be explained in text.

The sample at the end of the steel wire is surrounded by an alu-housing which will be heated together inside the quartz tube by an oven at 495° C. Argon atmosphere was used to prevent oxidation of the sample surface. After 45 minutes of equilibration, the housing together with the sample is dropped and the housing is blocked by the stopper. Meanwhile the sample moved continuously into the quenching bath of HCl solution (25 wt%) cooled to -70° C. This temperature was achieved by solidification of a certain amount of HCl with liquid nitrogen. Pre-cooling of the sample is prevented through the large heat capacity of the housing, thus a high quenching rate up to about 4×10^4 ° C /sec can be achieved [Ala82].

In this way by applying a series of improved techniques the influences from the thickness of the sample, pre-cooling and quenching medium on quenched-in vacancies concentration could be studied.

3.1.2. Pure Al Samples for PLS Measurements

Two pieces Al_AQ_HCL2 sample plates were treated in the same way as described before and used for the positron lifetime measurements.

3.1.3. AA7075 Samples for DBAR Measurements

6 samples of AA7075 were heated at 475° C for 45 minutes and quenched to achieve a super saturated solid solution state. Except 7075_AQ_HCl all other samples were quenched in water at RT. Four of them were aged at different temperatures for varying time as listed in Table 3.2. These heat treatments are performed to achieve maximal strength (T6) and to produce η´/η precipitates.

Sample	Heating	Quenching method	Aging
7075_AQ_HCl	475° C, 45 minutes	HCl solution at -70℃	no
7075_AQ_RT	475° C, 45 minutes	water at room temperature	no
7075_65_3	475° C, 45 minutes	water at room temperature	65° C, 3 hours
7075_130_3	475° C, 45 minutes	water at room temperature	130° C, 3hours
7075_130_12	475° C, 45 minutes	water at room temperature	130° C, 12 hours
7075_250_3	475° C, 45 minutes	water at room temperature	250° C, 3 hours

Table 3.2: Sample preparation for DBAR measurements of AA 7075.

The quenched-in vacancies will be trapped by solute atoms in this case and will prompt the formation of precipitates. The complicated operation described in section 3.1.1. is not essential due to the relative stable structure of the aged alloys, thus they can be measured in a simple way.

3.1.4. AA7075 Samples for XAS Measurements

For XAS measurement all samples were heated at 475° C for 1.5 hours, quenched in water at RT and aged under the same condition as described in section 3.1.3. Due to the long time required to travel to BESSY and the working schedule there, all samples were stored in liquid nitrogen in lab or inside a vacuum bottle filled with dry ice for transportation in order to prevent unwanted natural aging at room temperature. Sample details are given in Table 3.3:

Sample	Heating	Quenching method	Aging
7075_65_3	475° C, 1.5 hours	water at room temperature	65° C, 3 hours
7075_130_3	475° C, 1.5 hours	water at room temperature	130° C, 3hours
7075_130_12	475° C, 1.5 hours	water at room temperature	130° C, 12 hours
7075_250_3	475° C, 1.5 hours	water at room temperature	250° C, 3 hours

Table 3.3: Sample preparation for XAS measurements of AA7075.

3.2. Positron Lifetime Spectroscopy

3.2.1. Relevant Experimental Instruments

1) γ ray detector

Different γ ray detectors based on photoelectric effect and Compton scattering are required according to the method applied. For instance scintillation detectors with good time resolution are suitable for PLS measurement. Scintillation detectors consist of a scintillator from luminescent materials and a Photo Multiplier (PM) and coupled with related electronics. Electrons produced through photoelectric effect or Compton scattering from the incident γ ray will ionize and excite the atoms of the scintillator. The absorbed energy will be reemitted in the form of a weak flash of light through de-excitation, and these light signals will be collected, converted and amplified by the PM into appropriate electrical pulse for the consecutive analysis. The other type of γ ray detectors are the semi-conductor based detectors with good energy resolution. Electron-hole pairs generated in the p-n junction region by γ radiation drift to the electrodes under the electrical field and produce signals in the outer circuit. But this kind of detector should be cooled to about 77K with liquid nitrogen to avoid too much electrical noise since the thermal excited valence electrons are able to cross the band gap to the conduction band at higher temperature.

2) Constant Fraction Discriminator (CFD)

Output pulses from the PM vary in amplitude and rise time, which causes “time walk” problems of the consequent electronics [Leo87]. A Constant Fraction Discriminator is an electronic signal processing device designed to generate logic signals at a constant fraction of the peak height which will then be walk-free. This yields trigger times independently from peak heights.

3) Time to Amplitude Converter (TAC)

Time to Amplitude Converter is an instrument, which converts the time interval between two signals into a pulse with the amplitude proportional to the duration. The TAC will be triggered by a start pulse and ceased by a stop signal. The output pulse could be analyzed then by the MCA to give a spectrum as a function of the time interval. But there is a limitation in using such a instrument. This is the so called “dead-time”, which means that a time interval shorter than such dead-time will not be converted linearly. This problem can be solved through a delay lines added in front of the TAC for the coming signal. Meanwhile this enables the demarcation of the time interval by using different delay lines.

4) Single Channel Analyzer (SCA) & Multi Channel Analyzer (MCA)

The amplitude of the annihilation signal is proportional to the energy that is deposited in the detector by the photons. For positron annihilation technique the Single Channel Analyzer is used as a discriminator, which accepts only pulses with an amplitude within the fixed energy window. In this way only the desired nuclear events will be counted. Counts registered from different amplitudes (also called as channels) are accumulated to build up the complete energy spectrum, this can be achieved by a multi channel analyzer which scans the whole energy range and record the number of pulses counted in each channel.

3.2.2. Experimental Setup of PLS

The complete setup of positron lifetime spectrometer includes 3 main parts as shown in Fig. 3.5:

- Annihilation of positrons in sample and detection of the generated γ quanta (left part).
- Determination of the relevant signals with coincidence unit (middle part).
- Storage of annihilation events by MCA and computer (right part).

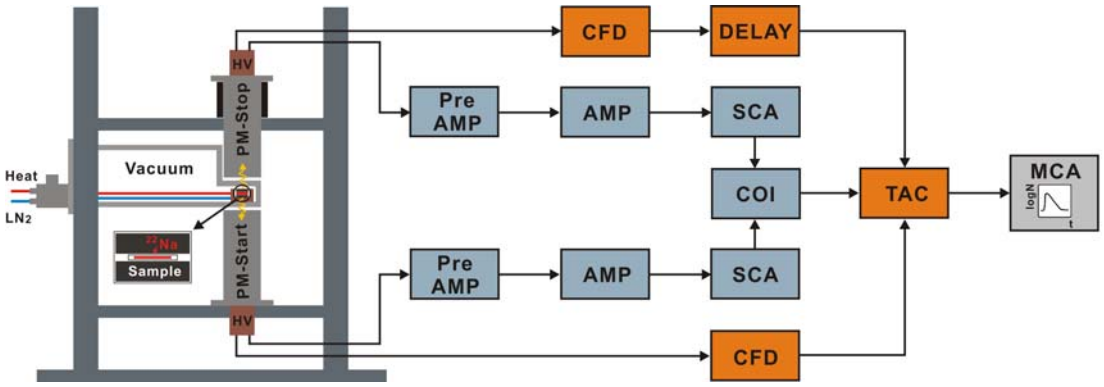

Fig. 3.5: Schematic diagram of "fast-slow" setup of PLS measurement. The fast channel is made up of CFD, delay line (which ensures that the TAC will work properly in the linear region) and TAC units used for the time measurement. The slow channel consists of amplifiers, SCAs (in order to suppress noise and accept input pulses within the energy window) and coincidence units, which are used for the energy selection of the γ quanta so that start channel allows only 1.27MeV γ free to enter as the start signal and only 0.511MeV γ as the stop signal for the stop channel.

A simple "sandwich" arrangement (this consists of two identical samples which envelope the ^{22}Na source) is used to ensure that all emitted positrons penetrate the sample material. In order to avoid confusions of the start and stop γ quanta from different annihilation events the activity of the source should be low.

γ quanta are collected and processed into electrical pulses by the scintillators and photo multipliers from both sides. These pulses are sent to the "fast-slow coincidence" unit in which two main parts are included, viz. the start channel at the bottom and the stop channel at the top, and each channel consists of another 2 sub-channels, the fast (red) and slow (blue) channel which work together as the coincidence unit. The fast channel is responsible for the time measurement between pulses (corresponding to the birth and annihilation γ quanta), which start and stop the TAC unit. The amplitude of the output pulse from TAC is then proportional to the time duration. These pulses are allowed to pass only after been determined by the slow channel as signals from the same annihilation event.

At least $3x10^6$ annihilation events should be registered in the memory of MCA after analog to digital conversion to obtain a reliable lifetime spectrum. An overview of the experimental setup is given in Fig. 3.6:

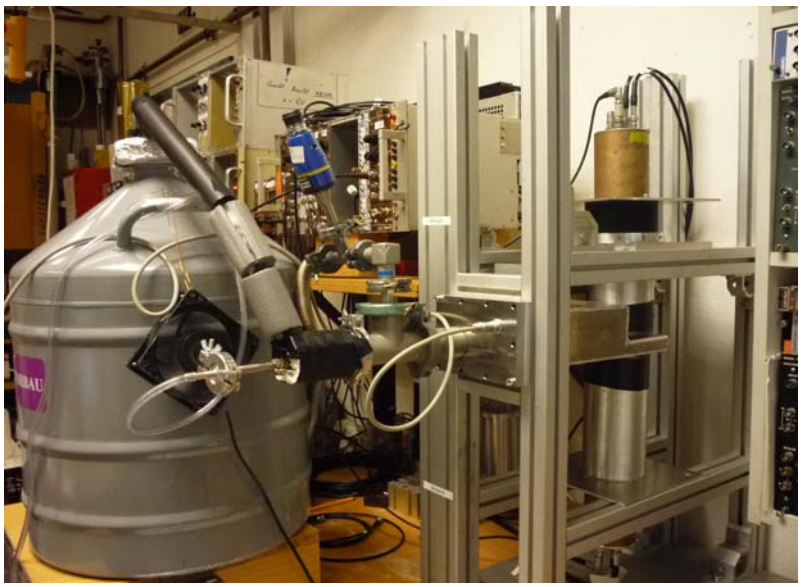

Fig. 3.6: An overview of the PLS experimental setup in the laboratory.

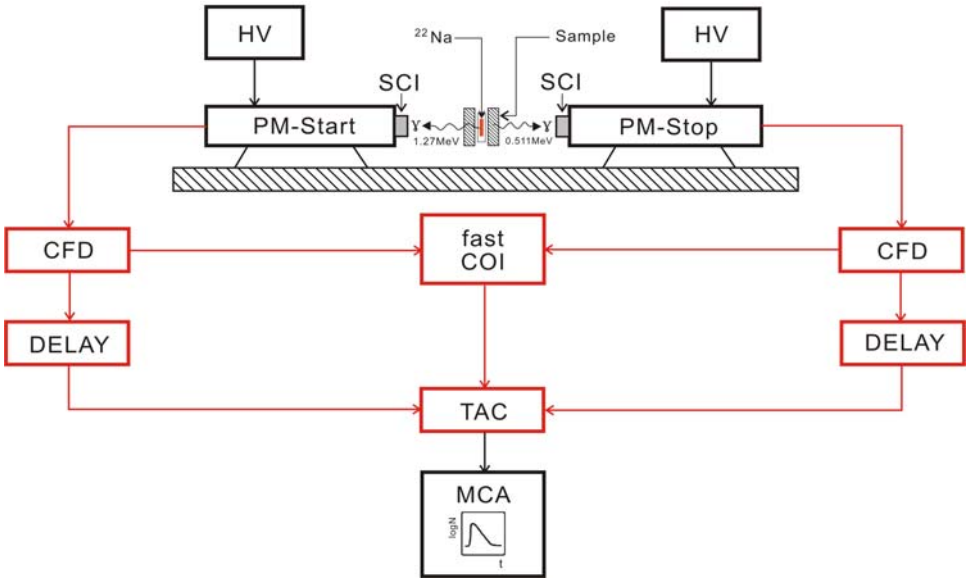

Fig. 3.7: Time spectroscopy using the CFD in a fast-fast timing System.

Besides its advantages, the count rate of the "fast-slow coincidence" setup is low and there are problems due to pileup of pulses. So the optimized "fast-fast coincidence" is widely used nowadays. In this case the "slow channel" is no more necessary since the CFD units are used not only for the time measurement but also the energy selection. The other parts remain basically the same, as illustrated in Fig. 3.7.

3.2.3. Time Calibration of the Spectrometer

The time corresponding to each channel can be calculated by the "delay line" method. A set of peaks of the time resolution curve can be measured with different delay lines and a plot of delay time versus the corresponding channel number provides then the channel width through formula t= △t / N, and in this study the channel width is calculated to be 25.2ps/channel.

3.2.4. Background Subtraction and Source Correction

To get a reasonable spectrum corrections of the experimental spectrum are required due to the contributions from background and annihilation events in the source. Since positrons annihilate not only in sample material but also in the source itself due to the way it was produced, namely, ^{22}NaCl salt wrapped inside Al foil (thickness in μm range), there are 3 lifetime components generally originating from: (1) annihilation in the salt source, (2) annihilation in Al foil, (3) formation of positronium between source and sample (which can be neglected in this study). The source correction used here is 420ps (source) and 215ps (Al foil) with the intensities 3% and 10%, respectively.

3.2.5. Analysis of PLS Spectra

The measured PLS spectra were analyzed using the software PAScual [Web10]. This software implements a Gaussian-like resolution function and different fitting procedures. Nevertheless, the measured spectra would be easily analyzed using standard least-square method.

3.3. Doppler Broadening Annihilation Radiation Spectroscopy

3.3.1. Experimental Setup of DBAR

The simplest form of the DBAR measurement employs a single Ge detector which allows data acquisition. Due to its background problem, the single detector DBAR technique provides very limited information about the core electrons that dominantly contribute to the high momentum part of the spectrum, i.e. the interesting and useful chemical information is lost. There are two possibilities to solve this problem. One is to use the Coincidence Doppler Broadening Spectroscopy [Kra99] and the other one employs only one detector but a sophisticated method of background subtraction. In this way almost the same information about the high momentum part can be obtained like those measured with two Ge-detectors. Additionally, this method is an optimal solution for geometrical problems, which prevent the arrangement of two collinear detectors.

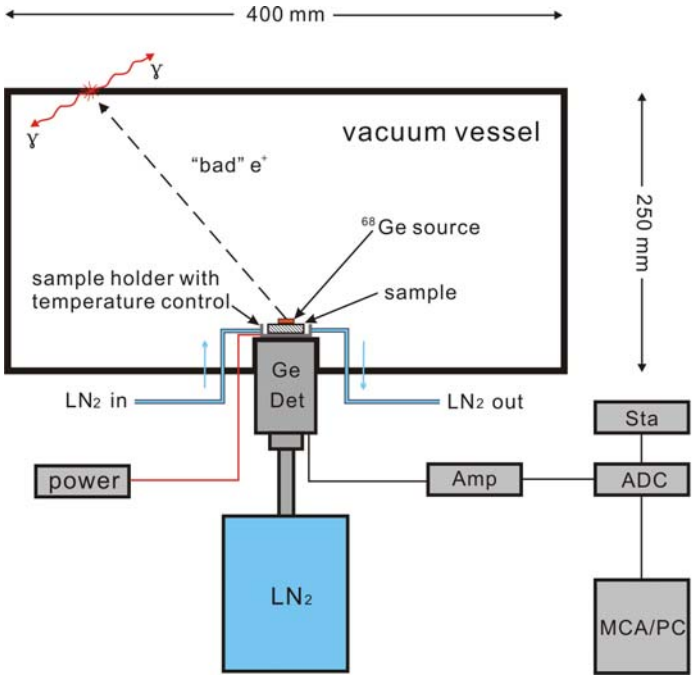

Fig. 3.8: Schematic diagram of the DBAR setup from which only one of the annihilation γ quanta will be detected. High purity Ge detector and spectra stabilization procedures are used.

The ^{68}Ge source was placed on the sample mounted in a sample holder with temperature control using liquid nitrogen and an additional heating wire. Beside the Germanium source, a Beryllium source was used for stabilization purposes. All samples were measured at -40^{o} C or -70^{o} C to avoid unexpected structural changes during measurement. The size of the large vacuum vessel is 400 mm in diameter and 250mm in height. Using such a design signals produced by those "bad" positrons from the top of the source will be avoided since they annihilate in a sufficient long distance in the walls of the vessel. Useful signals are collected through the high-purity Germanium detector. An amplifier was applied to process these signals after which were converted to digital signals by the ADC. Finally a MCA program was used to receive the processed signals [Haa06].

Fig. 3.9: An overview of the DBAR experimental setup in the laboratory.

3.3.2. Stabilization of the System

In order to measure tiny changes of the DBAR caused by structural changes, the Ge detector necessarily has to have a very good energy resolution, which in this case to be determined by the FWHM of the ^{7}Be photo peak (1.3-1.4keV in this study). In addition the stability of the energy resolution during the measurement should be considered because of two main reasons:

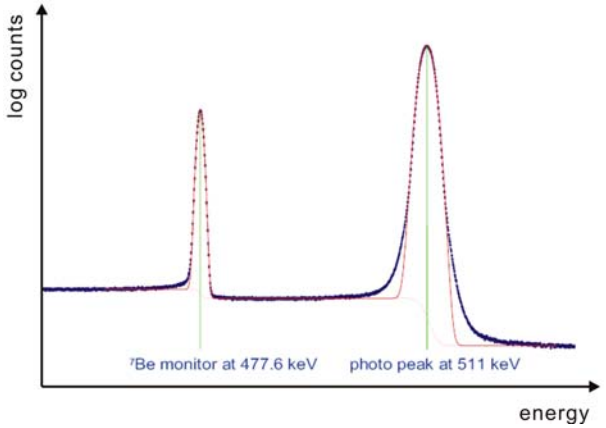

Fig. 3.10: Energy spectrum and software correction of long-term drift of the electronics [Haa06].

- Long-term instabilities of the electronics due to temperature changes in the surrounding. Such influences are corrected after the measurement by determination of the centers of the monitor line and the annihilation peak for all separately recorded spectra. These spectra are saved every 10 minutes and added according to a two-point zero/gain correction afterwards.

- Short-term drifts in the electronics. The gain of the ADC is stabilized with the single-point hardware stabilization of the ^{7}Be monitor line (477.6keV), which is measured simultaneously with the ^{68}Ge photo peak, as demonstrated in Fig. 3.10.

2 digital windows are selected (±5 channels, ±10channels around ^{7}Be line) and the ratio △N (N_1 / N_2) of the counts from each window should be constant if the system is stable. In case of drifts the variation of △N results in a voltage fluctuation △V, which will be used as a feedback to stabilize the system, as illustrated in Fig. 3.11:

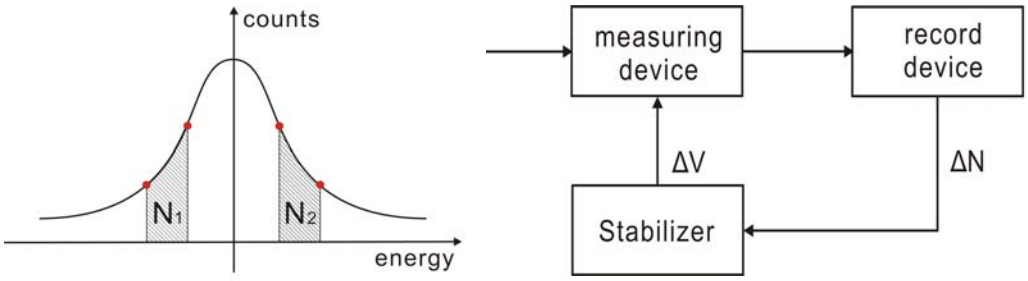

Fig. 3.11: Principle of the stabilization

After the long and short-term correction a minimum broadening of the spectrum is achieved.

3.3.3. Efficiency Correction

Efficiency correction is applied as the first step of the data treatment to avoid unphysical spectra, since the efficiency of the Ge-detector is a nonlinear function of energy. ^{152}Eu has a gamma spectrum from 121.8 to 1407.5keV with well-known relative intensities, which can be used to determine the energy -dependent efficiency of the detector [Son02].

E [keV]	Channel	I_{Lit}	I_{Mes}
121,78	558,42 ± 0,02	1360	6778 ± 100
244,93	1127,70 ± 0,02	359	1460 ± 18
344,47	1588,91 ± 0,02	1280	3961 ± 47
444,08	2050,68 ± 0,02	148	373 ± 4
778,87	3602,18 ± 0,02	622	988 ± 11
867,83	4012,01 ± 0,02	199	293 ± 3
963,93	4459,95 ± 0,02	693	944 ± 10
1085,60	5024,29 ± 0,02	475	598 ± 7
1111,85	5145,83 ± 0,03	649	777 ± 9
1407,54	6517,14 ± 0,02	1000	1000 ± 11

Table 3.4: Measurement of the rel. efficiency.

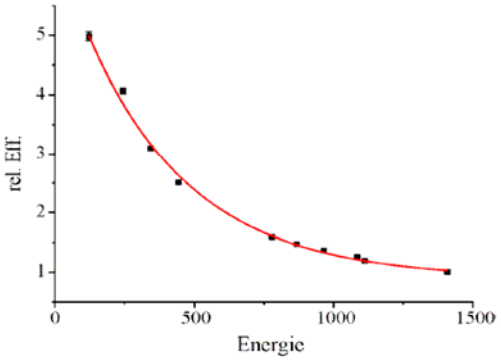

Fig. 3.12: Energy dependent rel. efficiency.

Around the 511keV energy peak the efficiency is given analytically as eff (E) = A_1+A_2 exp (-E/A_3), where A_1 = 0.90 ± 0.02keV, A_2 = 5.67 ± 0.09keV, A_3 = 374 ± 8keV is found for the used detector [Haa06], and the real intensity is then calculated as the ratio of the measured intensity I_{Mes} to the efficiency eff (E). Due to this reason all spectra are necessarily to be corrected before next step, namely background subtraction.

3.3.4. Background Subtraction

Statistical fluctuations originating from Ge-detector, amplifiers and ADC lead to the broadening of the γ peak, therefore the total line width of the 0.511MeV annihilation peak consists of not only the Doppler broadening but also the Gaussian noise. Additionally, backgrounds should be subtracted to extract real information form the spectrum. There are mainly three types of background, as indicated in Fig. 3.13 [Haa06]:

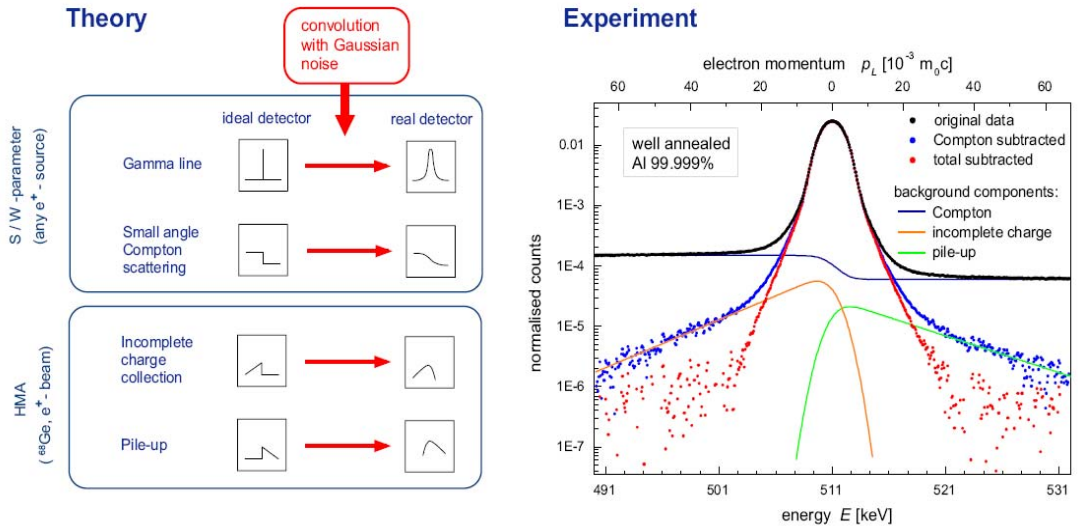

Fig. 3.13: Subtraction of the annihilation spectrum consisting 3 background components.

- High-energy background radiation from decays of natural isotopes in the surrounding and also inside the source with energies above 511keV, but for the source isotope ^{68}Ge used for Doppler broadening spectroscopy this contribution is very small compared to ^{22}Na.
- A step-like Compton background with the edge located at 0.511MeV caused by small angle Compton scattering with minimal energy transfer. These events occur between the annihilation γ and the detector, sample, walls of the sample holder/detector. The energy loss leads to the step-like background convoluted with the photo peak.
- Tails at the low/high energy side are induced from incompletely free charge collection in the detector and pile-up problems even at low counting rates (the counting rates at the annihilation peak is kept around 1200cps in order to avoid further broadening of the peak), accordingly. Distribution of both tails should be almost symmetrical in case of a good adjustment of the amplifier.

The background subtraction can mathematically be represented by formula:

$$P(E) = a_G e^{(-u^2)} + \frac{a_S}{2}\left[1 - erf(u)\right] + \frac{a_L}{2} e^{(-\mu_L u)} \cdot \left[1 - erf(u)\right] + \frac{a_H}{2} e^{(\mu_H u)} \cdot \left[1 + erf(u)\right] + b$$
$$u = 2\sqrt{\ln 2}(E - E_0)/\sigma \qquad (3.1)$$

The peak and background is described by P(E) as a function of the energy, erf is the error function, σ is the FWHM of the Gaussian, E_0 is the center of the peak, $a_{G/S/L/H}$ indicates the amplitude of the Gaussian, step function, low / high energy tail, respectively, $\mu_{L/H}$ is the slope of the low/high energy tail and b is the constant background.

The different terms in formula 3.1 represent the contributions from photo peak, step function, low/high energy tails and natural background correspondingly, which finally build up the total spectrum. The results subtracted after different steps are graphically illustrated in Fig. 3.14 by different colors and the red spectrum shows the final spectrum.

By using computer program “M_SPEC” developed by M. Haaks both corrections of the efficiency and background are realized [Haa08].

3.4. X-ray Absorption Spectroscopy

3.4.1. Experimental Setup of XAS

The XAS measurement was carried out at BESSY using the 7T-MPW-magS beamline in order to obtain the complementary information about the environment of the specific element. An overview of the experimental setup is shown in the figure below:

Fig. 3.14: An overview of the XAS experimental setup at BESSY. Two major parts are included, i.e. optical system of the beamline (right side) and detecting system of the fluorescence (left side).

3.4.2. Experimental Procedure

The XAS measurements were performed in the following steps:

(1) First of all the sample was mounted on the sample holder. On the left side a 0.5mm thick Zn foil (purity 99.999) was used as the reference (see Fig. 3.15). They were mounted on a cryostat capsuled by a beryllium cap and cooled to 173K afterwards.

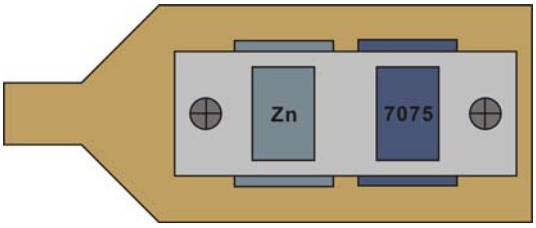

Fig. 3.15: Sample arrangement of XAS measurement.

(2) The x-ray energy was set to 9670keV and by driving the position motor horizontally from left to right hand side the first scan was made to find the positions of the reference and the sample.

(3) Position motor was moved and stopped at the Zn position. The counts from detector should be checked and modified to the value of 110000 roughly, which ensures a linear behavior of the detector. An energy scan around Zn K edge (9659keV) was used for the energy calibration.

(4) Then the position motor was moved to the sample position if everything is ok and counts was controlled again. Before next energy scan an additional angle scan was carried out from about 87^{o} to 93^{o} to check the positions of Bragg-peaks which could affect the result probably. But by selecting the proper angle between these peaks such problem was solved.

(5) Until this step nearly everything is ready but a coarse energy scan in the range from 10345 to 9500keV was executed as a general view. If nothing serious happens the real energy scan can be performed now. The energy range was divided into three parts according to its importance, namely:

- 10345keV-10145keV in 200 steps
- 10144keV-9645keV in 1000 steps
- 9640keV-9500keV in 28 steps

Such an energy scan was repeated twice for better statistics.

(6) After the measurement the system was set to 280K and de-evacuated.

The program used for sample 65_3 is included in appendix A.4.

Chapter 4
Results and Discussions

4.1. EDX Measurements of AA7075 Elemental Concentration

An Energy Dispersive X-ray (EDX) analysis was perfomed in order to identify the alloying elements of AA7075 and their corresponding concentrations. In general, it works in the following way: core electrons are knocked of the sample material by bombarding electrons and holes are created, which will be occupied by another electron from an outer shell. The excessive energy will be released in the form of element specific x-ray fluorescence radiation, thus the identification of element composition can be obtained. Four measurements at different sample locations were made to account for possible local fluctuations. Their average values are supposed to represent the actual composition. An exemplary measurement is shown below:

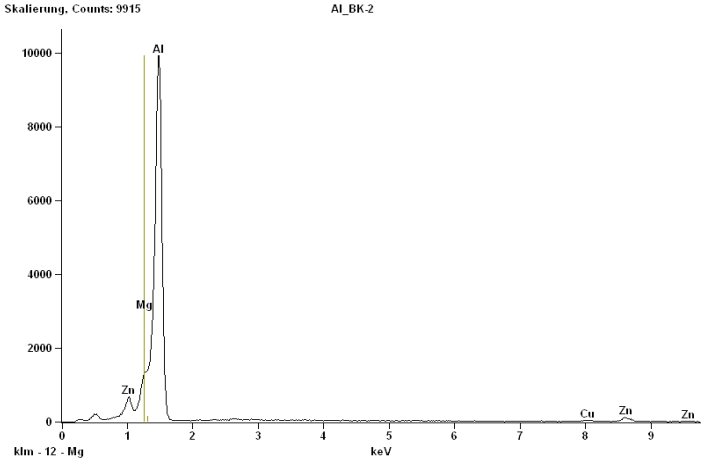

Fig. 4.1: A single EDX measurement of the AA7075 sample.

The elemental concentration obtained by this measurement is:

Element Linie	K-Verhältnis	Gew.-Konz %	Gew. % Fehler	Atom Konz %	Atom- % Fehler	Formel
Mg K	0.06	6.12	+/- 0.33	7.06	+/- 0.38	Mg
Al K	0.86	86.36	+/- 0.45	89.70	+/- 0.46	Al
Cu K	0.01	1.31	+/- 0.12	0.58	+/- 0.05	Cu
Zn K	0.07	6.21	+/- 0.37	2.66	+/- 0.16	Zn
Total		100.00		100.00		

Table 4.1: Alloying elements concentration by one measurement.

The average values are: Cu concentration = 1.5% (wt%), Zn concentration = 5.7% (wt%), which are in good agreement with the data sheet (Table 2.2). But due to the adjacent atomic number of Al and Mg, the measured Mg concentration is invalid, which is especially problematic in the case of low Z elements. Anyway, it is in the range of 2.1-2.9% (wt%).

4.2. DBAR Measurements of Quenched-in Vacancies in Pure Al

DBAR ratio-plots of different quenching procedures carried out with pure aluminium are shown in Fig. 4.2. Since all samples were made from pure aluminium (5N), the DBAR signal originates only from the vacancy like defects.

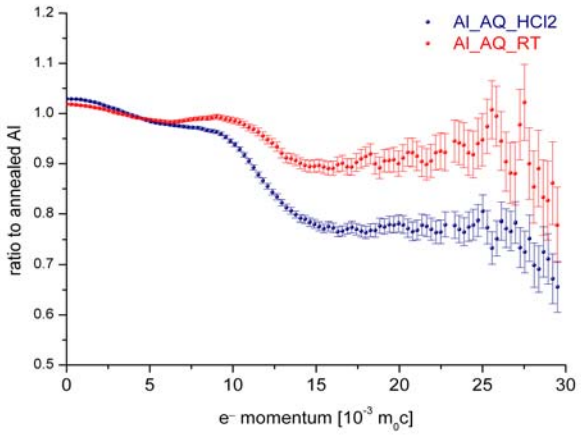

Fig. 4.2: Ratio-plots of the sample Al_AQ_RT vs. Al_HCl2.

Ratio-plots of the samples Al_AQ_RT and Al_AQ_HCl2 are shown in Fig. 4.2. Obvious differences in the low and high momentum region arise mainly from the optimized quenching method with the HCl solution at –70° C, and in addition from those efforts which kept the sample sufficiently cold before or during the measurement. Therefore, this result indicates that quenching to RT and handling the sample at RT lead to significant decrease of vacancy concentration, although the whole procedure at RT took about 4.5 minutes only.

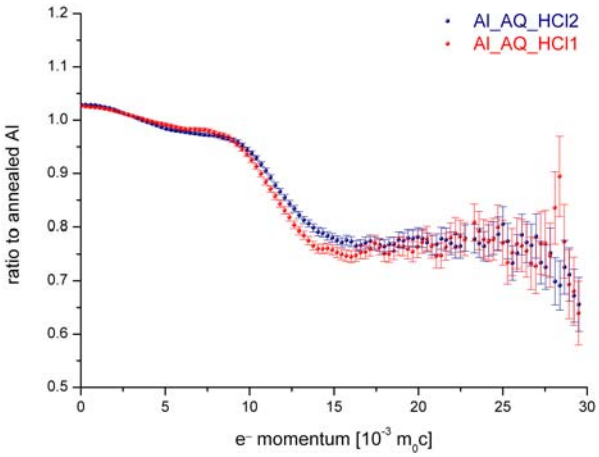

Fig. 4.3: Ratio-plots of the sample Al_AQ_HCl1 vs. Al_AQ_HCl2.

Ratio-plots of Al_AQ_HCl1 and Al_AQ_HCl2 are essentially the same, which means that the influence from sample thickness and pre-cooling prevention during quenching is not dominant in the quenching process. The deviation is probably due to the evaluation process and can be neglected. Nevertheless, it should be noticed that in both cases the sample is actually small and the fall distance is also relative short, thus they can be efficiently quenched to –70° C in short time. But in case of larger geometry and longer fall path these parameters are believed to affect the concentration of quenched-in vacancies.

By using the DFT code SIESTA, the relaxed coordinates of a single vacancy in pure aluminium matrix were calculated and on this basis a simulation of the DBAR signal was carried out [Kor07]. The simulation result (energy resolution 1.4 keV) is compared to the sample Al_AQ_HCl2 in Fig. 4.4:

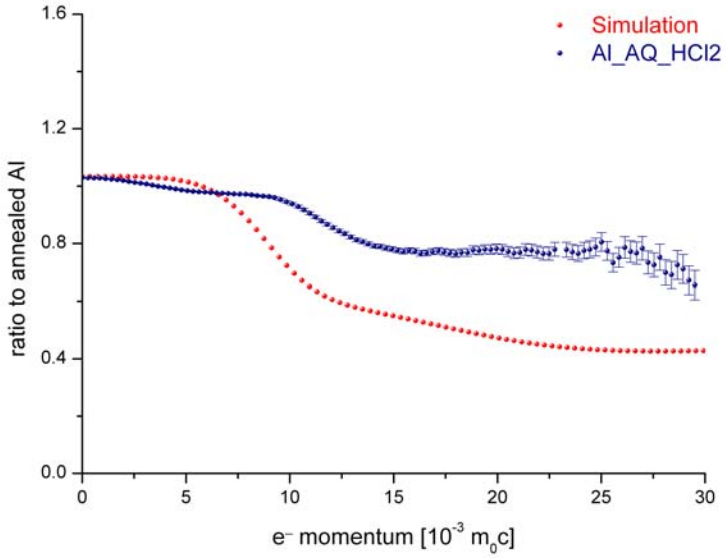

Fig. 4.4: Ratio-plots of simulation result vs. Al_AQ_HCl2.

Generally the structure form both is in good agreement except the deviation in the high momentum region.

(1) The difference in the momentum region from $5x10^{-3}m_oc$ to $10x10^{-3}m_oc$ is on account of a systematic error of calculation. The wave function of valence electrons is calculated only for a free atom in the model but actually due to atomic superposition it is not the case in reality [Kor07].
(2) The difference in the momentum region from $10x10^{-3}m_oc$ to $30x10^{-3}m_oc$ is probably due to the incomplete positron trapping which could be verified by PLS measurement. (see next section)

Nevertheless, it should be stressed that the curvature of the simulation in the high momentum agrees very well with the experimental one.

4.3. PLS Measurement of Quenched-in Vacancies in Pure Al

This PLS measurement was performed in order to verify our hypothesis from last section. Two sample plates of Al_AQ_HCl2 were heated at 495° C for 45 minutes, quenched in HCl at -70° C and then measured at the same temperature.

Two lifetime components are obtained through a non-linear fit (χ^2 = 1.0828), viz. τ_1 and τ_2 corresponding to a reduced bulk lifetime and a vacancy component, respectively, as shown in Table 4.2 (all τ has unit of ps). The resolution function is 278ps in this study.

τ_1	τ_2	I_1	I_2
80	238	0.395	0.605
$\Delta\tau_1$	$\Delta\tau_2$	ΔI_1	ΔI_2
3	1	0.006	0.006

Table 4.2: Fitted lifetime components and the relative intensities.

The positron bulk lifetime can be calculated by equation below [Kra99]:

$$\tau_b^{calc} = \left(\sum_{j=0}^{k} I_j \lambda_j \right)^{-1} = \left(\sum_{j=0}^{k} I_j / \tau_j \right)^{-1} \tag{4.1}$$

τ_b^{calc} is about 134ps from this measurement, compared to 156ps (value from experiments before) this result is acceptable. The specific trapping rate μ used for the following calculation was 10^{14}/second. All calculated results are listed in Table 4.3:

$\tau_{average}$	κ [1/s]	conzentration	η [%]	τ_b^{calc}
176	5.02E+09	5.02E-05	43.9	133.7
$\Delta\tau_{average}$	$\Delta\kappa$	Δ conzentration	$\Delta\eta$	$\Delta\tau_b^{calc}$
2	4.16E+09	4.16E-05	0.5	0.7

Table 4.3: Calculated lifetime components and the relative intensities.

The trapping rate κ is $5x10^9$/sec roughly, thus the vacancy concentration in the quenched sample is calculated to be about $5x10^{-5}$/atom according to equation (2.7). The annihilation fraction η is about 44% according to equation (2.8). This indicates an incomplete positron trapping, which leads to the difference between the simulation and experimental ratio-plots in Fig. 4.4.

Finally the ratio-plot of Al_AQ_HCl2 was re-calculated in order to get the "real" ratio-plot. This was achieved by the equation below:

$$Ratio_{\exp} = \eta \cdot Ratio_{real} + (1-\eta) \cdot Ratio_{bulk} \qquad \text{where Ratio}_{\text{bulk}} = 1 \tag{4.2}$$

The ratio-plot is re-plotted in Fig. 4.5 as below:

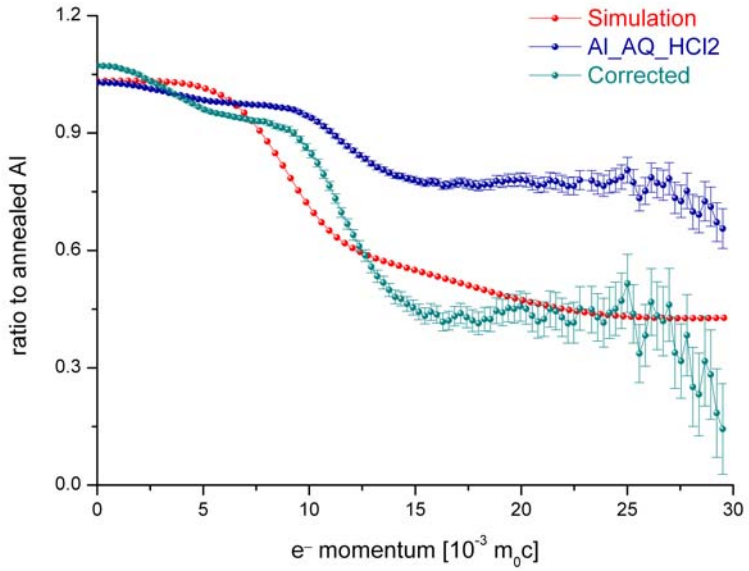

Fig. 4.5: "real" ratio plot compared to simulation result.

The corrected plot is in good agreement in the high momentum region with the simulation. Deviations in the low momentum region are mainly caused by calculation errors. Nevertheless it is remarkable that experiment and simulation agree in the region of very high momentum (from $20x10^{-3}m_0c$ to $27x10^{-3}m_0c$).

4.4. DBAR Measurements of Precipitation in AA7075

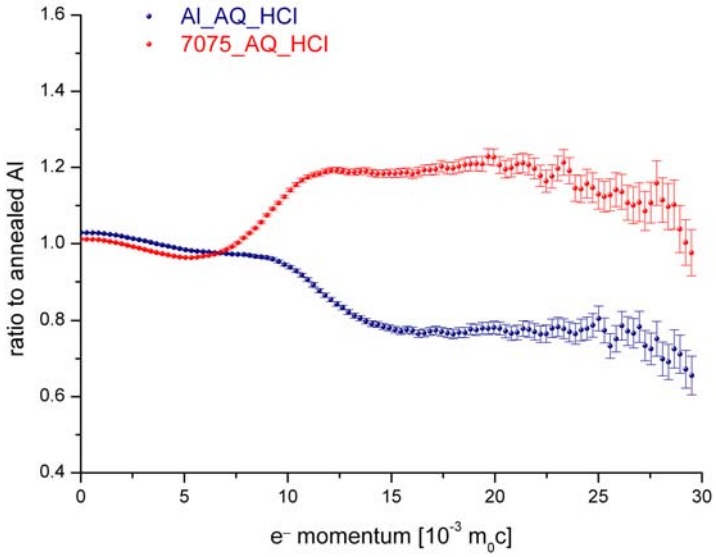

Fig. 4.6: Ratio-plots of AA7075 compared to pure Al.

Compared to the ratio-plots of pure aluminium, AA7075 sample presents a different momentum distribution (See Fig. 4.6), especially at the high momentum region due to one or more alloying atoms e.g. Zn / Cu atoms around vacancies, thus the presence of alloying atoms can be measured by DBAR spectroscopy very effectively.

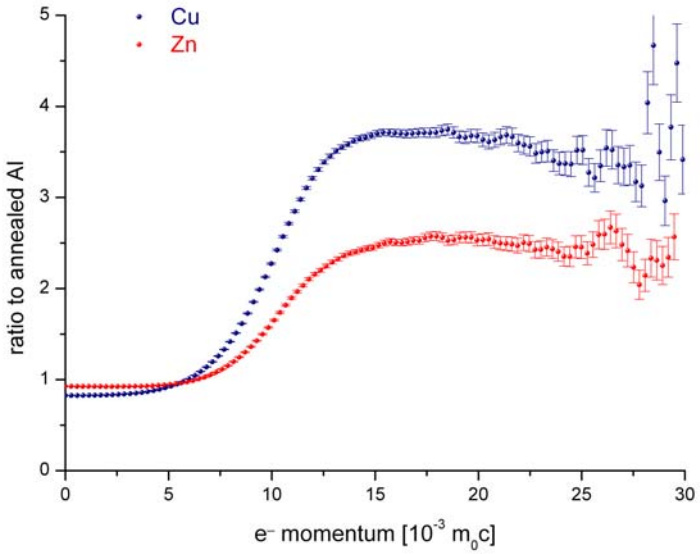

Fig. 4.7: Ratio-plots of pure transition metals Zn and Cu.

Typical ratio curve of pure Zn and Cu relative to well-annealed aluminium are shown in Fig. 4.7. The main differences between these transition metals and aluminium originate from their electronic configuration, for instance the hutch structure of Cu curve located around $15x10^{-3}m_0c$ is caused by the annihilation of positrons with 3d electrons. In this study the change in the high momentum region compared to pure aluminium is caused by the relative high concentration of Zn atoms (see Fig. 4.6).

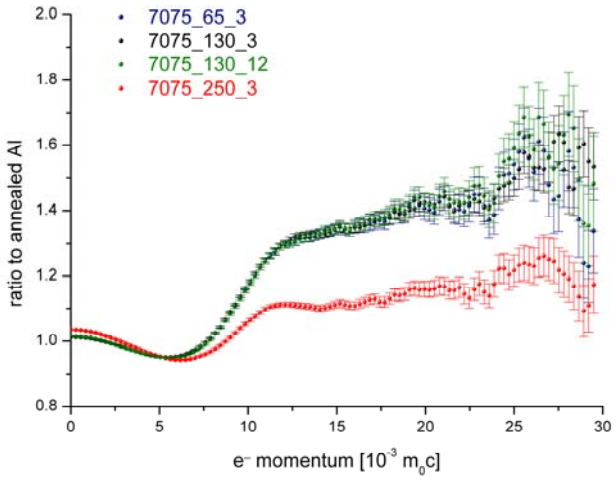

Fig. 4.8: Ratio-plots of AA7075 sample aged under different conditions.

Ratio-plots of AA7075 samples aged at 65° C , 130° C, 250° C for 3 hours and 130° C for 12 hours are given in Fig. 4.8. According to Dlubek complete positron trapping can be assumed in this situation [Dlu98]. Curves of 7075_65_3, 7075_130_3 and 7075_130_12 are more or less identical, which signifies similar surroundings of vacancies. By increasing the aging temperature to 250° C the alloying atom concentration around vacancies begins to decrease due to formation of η and / or η´ precipitates, which is indicated by the decrease in the high momentum region. Samples 7075_130_3 and 7075_130_12 should have presented alterations in the ratio plot since formation of η´ phase under the corresponding aging conditions [Buh08] leads to positron trapping at the phase boundaries. However, no change was observed. Thus we deduce that η´ precipitates are not dominantly responsible for the strengthening.

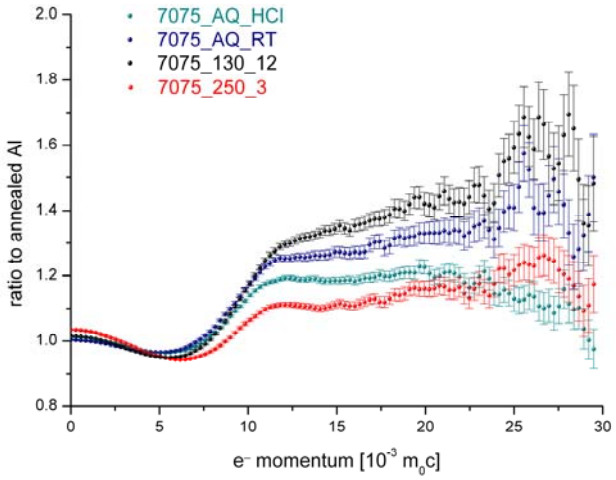

Fig. 4.9: Ratio-plots of as quenched and aged AA7075 samples.

Samples quenched with HCl at -70° C and water at RT are compared to aged samples as well. The changes in high momentum region of the sequence 7075_AQ_HCl → 7075_AQ_RT → 7075_130_12→7075_250_3 depends on the solute atom concentration around vacancies, which increases during low temperature aging, and decreases due to formation of η´/η preicpitates afterwards. The difference between 7075_AQ_HCl and 7075_AQ_RT can moreover be attributed to a incomplete positron trapping at the very beginning of aging, which was observed for Al-Mg-Si and Al-Cu-Mg alloys [Klo07].

4.5. XAS Measurement of Precipitation in AA7075

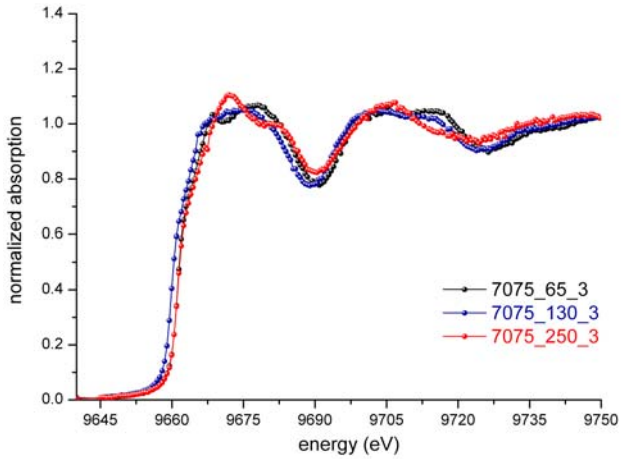

Fig. 4.10: XANES spectra of AA7075 samples.

Results of the x-ray absorption near edge structure of AA7075 samples aged at 65° C, 130° C and 250° C for 3 hours after quenching at RT are illustrated in Fig. 4.10. All spectra (processed with the software package Athena) were normalized to the edge height and exhibit very broad white line (increase of absorption directly after the absorption edge). The spectra of samples 7075_65_3 and 7075_130_3 are basically identical, but different from sample 7075_250_3, in which a kink on the right shoulder of the white line is included. Additionally shift of Zn K edge and noise are also included in the spectra.

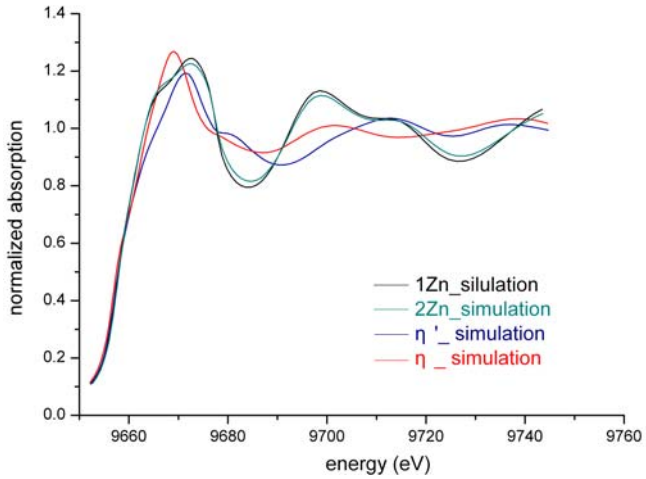

Fig. 4.11: FEFF calculation of Zn K-edge under different models.

Comparison between measured and calculated reference spectra is required for analysis of XANES spectrum. By applying the FEFF8 code numerical simulations were performed to obtain the Zn K-edge XANES under different circumstances, viz, one single Zn atom and two Zn atoms embedded in the Al matrix as well as η´ and η precipitates, the structures of η´ and η taken from [kve06][Web7] were processed on line [Web11]. Beside the difference between all simulations the similarity from first two spectra (1 Zn atom & 2 Zn atoms) indicates that small agglomerates of Zn atoms has nearly no influence on the near edge structure. Moreover, it can be concluded that a broad white-line is an indication of small agglomerates in Al-Zn-Mg.

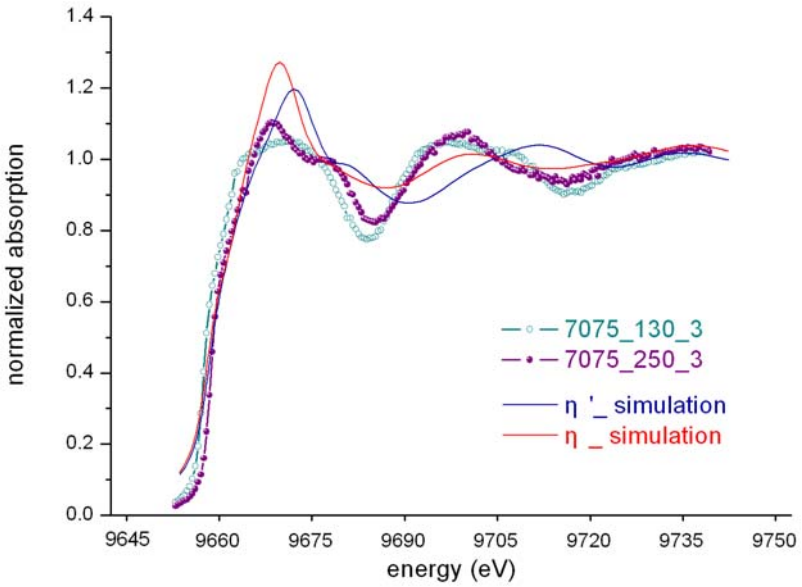

Fig. 4.12: Comparison of the measured and calculated XANES spectra.

All calculated absorption edges in Fig. 4.12 have larger amplitudes than the measured ones, since broadening was not considered for the simulation. The measured spectrum of 7075_250_3 could be imagined as combination of the calculated spectra of η´ and η, especially due to white line and the kink on the right shoulder, therefore we deduce that sample 7075_250_3 contains both η´ and η precipitates. Meanwhile no obvious resemblance was found between the measured spectrum of 7075_130_3 sample and the simulations, thus the following comparison was made as shown in the following figure:

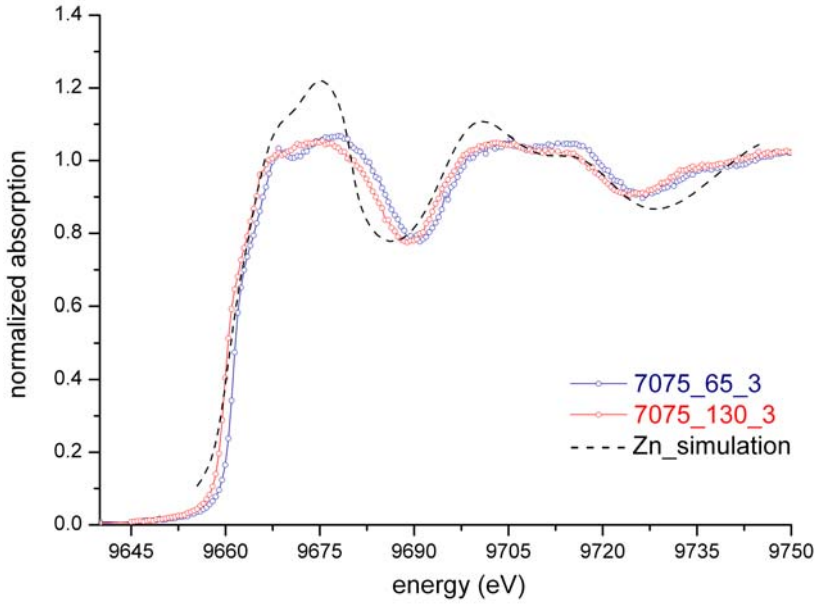

Fig. 4.13: Comparison of the measured and calculated XANES spectra.

The measured spectra of sample 7075_65_3 and 7075_130_3 are in good agreement of the calculated 1 Zn or 2 Zn spectra, which provides further evidences for the DBAR measurement, namely, there are no significant presence of η´ precipitates at 130^{o} C but small agglomerates of Zn atoms.

Chapter 5
Conclusions

The quenched-in vacancies in pure aluminium and formation of precipitates during aging of AA 7075 were investigated by means of Doppler Broadening Annihilation Radiation spectroscopy and Positron Lifetime Spectroscopy techniques. In addition, X-ray Absorption Near Edge Structure measurements were performed in order to obtain complementary information.

Compared to the conventional method an optimized quenching technique was applied to freeze thermal vacancies in pure aluminium, including new quenching medium (HCl solution at –70° C) and pre-cooling prevention. Experimental results show that a considerable fraction of quenched-in vacancies could be measured efficiently under such conditions with the DBAR technique, while quenching and handling the sample at room temperature leads to significant decrease of vacancy concentration, although the whole procedure at room temperature took about 4.5 minutes only. In addition, thickness and pre-cooling prevention during quenching is not dominant, this is valid for those samples of small size at least.

Comparison between simulation and experiments of ratio-plots shows good agreement besides deviation in the high momentum region originating from incomplete positron trapping, which was tested by positron lifetime spectroscopy measurement afterwards. Results show a vacancy concentration of $5x10^{-5}$/atom and a vacancy related lifetime about 240ps for the pure aluminium sample quenched in HCl at -70° C. The annihilation fraction was calculated to be about 44%, indicating an incomplete positron trapping. Therefore the inference mentioned above was verified. The corrected ratio-plots match very well with the simulation.

Not only pure aluminium but also AA7075 was investigated in this study by means of DBAR technique. Samples aged at 65° C for 3 hours, 130° C for 3 and 12 hours after quenching behave similarly in the ratio-plots, indicating no presence of η´ precipitates, which are commonly believed to be formed at such aging conditions and to dominantly influence the strengthening of the alloy. Therefore from a vacancy perspective one can conclude that η´ is not significantly formed at the mentioned aging conditions. In addition, AA7075 sample aged at 250° C shows big difference compared to other ratio curves due to formation of η´ and or η precipitates which could be easily observed. Combined with samples quenched in water (RT) and HCl (–70° C), the increase of alloying atoms concentration around vacancies during low temperature aging and the subsequently decrease due to formation of precipitates can be clearly distinguished as well.

Further investigations were performed in order to provide evidence for our inference by utilizing XANES technique. Samples aged at 65° C, 130° C and 250° C for 3 hours after quenching were measured and compared to calculated reference spectra consequently. Results from the comparison reveal that sample aged at 250° C contains both of η´ and η precipitates. Meanwhile spectra of the aged samples at 65° C / 130° C and the calculation of small agglomerates of Zn atoms embedded in Al matrix are in good agreement, which provides us further evidence of the previous assumption from DBAR experiment, viz. no significant presence of η´ precipitate by aging at 130° C for 3 hours but just small agglomerates of Zn atoms.

References

[Ala82] A. Alam and r.N. West. Positron Studies of Vacancy Clustering in Quenched Aluminium and Dilute Aluminium Alloys. J. Phys. F: Met. Phys. 12: 389-97 (1982).

[And33] C.D. Anderson. The Positive Electron. Physical Review **43** (6): 491–494 (1933).

[And06] Andreas Riedl and Jonny Ulrich. Studienarbeit: Werkstoffdaten. Fahrzeugtechnik, HS-Ulm (2006).

[Bon]V. Bondarenko and R. Krause-Rehberg. Study of Semiconductor with Positron. Martin-Luther-University Halle-Wittenberg, Germany.

[Buh08] J. Buha, R.N. Lumley and A.G. Crosky. Secondary Ageing in an Aluminium Alloy 7050. Materials Science and Engineering A 492: 1-10 (2008).

[Cla05] B.G.Clark, I.M. Robertson and L.M. Dougherty. High-temperature Dislocation Precipitate Interactions in Al Alloys. J. Mater. Res., Vol. 20, No. 7: 1792-1801 (2005).

[Dlu98] G. Dlubek, p. Lademann, H. Krause, S. Krause and R. Unger. Positron Lifetime Studies of Decomposition in 2024 (Al-Cu-Mg) and 7010 (Al-Zn-Cu-Mg) Alloys. Scripta Materialia, Vol. 39, No. 7: 893-899 (1998).

[Dup04] A. Dupasquier, G. Kögel and A. Somoza. Studies of Light Alloys by Positron Annihilation Techniques. Acta Materialia 52: 4707-4726 (2004).

[Fri26] J.B. Friauf. The Crystal Structure of $MgZn_2$. California Institute of Technology (1926).

[Got98] G. Gottstein. Physikalische Grundlagen der Materialkunde. Springer Verlag (1998).

[Gre97] H. Greif, M. Haaks, U. Holzwarth, U. Männig, M. Tongbhoyai, T. Wider and K. Maier. High Resolution Positron-Annihilation Spectroscopy with a New Positron Microprobe. Appl. Phys. Lett., Vol. 71, No. 15 (1997).

[Haa84] P. Haasen. Physikalische Metallkunde. Springer-Verlag (1984).

[Haa03] M. Haaks. Positronenspektroskopie an Ermüdungsrissen und Spanwurzeln. Dissertation, Rheinische Friedrich-Wilhelms-Universität Bonn (2003).

[Haa06] M. Haaks, T.E.M. Staab and K. Maier. Analyzing the High-Momentum Part of Positron Annihilation Doppler Spectra with a Single Germanium Detector. Nuclear Instrument and Methods in Physics Research A 569: 829-836 (2006).

[Haa08] M. Haaks and T.E.M. Staab. High-momentum Analysis in Doppler Spectroscopy. Applied Surface Science. Vol. 255, Issue 1: 84-88 (2008).

[Jac] M.H. Jacobs, Phase Transformations in Metals and Alloys. The University of Birmingham (1992).

[Kar04] G.P. Karwasz, A. Zecca, R.S. Brusa and D. Pliszka. Application of Positron Annihilation Techniques for Semiconductor Studies. Journal of Alloys and Compounds 382: 244-251 (2004).

[Klo07] B. Klobes. Untersuchungen zu Frühstadien der Ausscheidungsbildung in AlMgSi -Legierungen. Helmholtz Institut für Strahlen- und Kernphysik, Uni Bonn (2007)

[Kor07] B.Korff. Simulation von Parametern der Positronenannihilation in Aluminium -Legierungen. Helmholtz Institut für Strahlen- und Kernphysik, Uni Bonn (2007).

[Kra99] R. Krause Rehberg and H.S. Leipner. Positron Annihilation in Semiconductors. Springer-Verlag (1999).

[Kve06] A. Kverneland, V.Hansen, R.Vincent, K.Gjonnes and J. Gjonnes. Structure Analysis of Embedded Nano-Sized Particles by Precession Electron Diffraction. η´- Precipitate in an Al-Zn-Mg Alloys as Example. Ultramicroscopy 106: 492-502 (2006).

[Len76] B. Lengeler. Quenching of High Quality Gold Single Crystals. Philosophical Magazine, Vol. 34, No. 2: 259-264 (1976).

[Leo87] W.R. Leo. Techniques for Nuclear and Particle Physics Experiments. Springer-Verlag (1987).

[Liv84] R.J. Livak and J.M. Papazian. Effects of Cupper on Precipitation and Quench Sensitivity of Al-Zn-Mg Alloys. Scripta Metallurgica, Volume 18, Issue 5: 483-488 (1984).

[Lrp] Positron Annihilation Lifetime Spectroscopy, Principles and Applications for Nano Science. Laboratories for Radiation & Polymer Science (LRPS) of the Department of Chemistry, Hacettepe University, Turkey

[Mar06] R.K.W. Marceau, N. Tsafant, P. Liddicoat, G. Sha and S.P. Ringer. Thermal Impact on Laboratory-Scale Heat Treatment Samples During Elevated Temperature Aging for Short Duration. Australian Key Center for Microscopy and Microanalysis, The University of Sydney (2006).

[Meh00] Jagdish Mehra and Helmut Rechenberg. The Historical Development of Quantum Theory, Vol. 6: The Completion of Quantum Mechanics 1926–1941:804 (2000).

[New08] M. Newville. Fundamentals of XAFS. Consortium for Advanced Radiation Sources. University of Chicago, Chicago, IL (2008).

[Now07] C. Nowill. Investigation of the Quench and Heating Rate Sensitivities of Selected 7000 Series Aluminum Alloys. Worcester Polytechnic Institute (2007).

[Pro01] I. Prochazka. Positron Annihilation Spectroscopy. Materials Structure, Vol. 8, No. 2 (2001).

[Sme] L.C.Smedskjaer and M.J. Fluss. Experimental Methods of Positron Annihilation for the Study of Defects in Metals. Materials Science and Technology Division, Argonne national Laboratory, lllnois.

[Son02] S. Sonneberger: Verformungsverhalten von Technischen Aluminiumlegierungen, Diplomarbeit, Uni Bonn (2002).

[Sta08] T.E.M. Staab, M. Haaks and H. Modrow. Early Stages of Aluminium Alloys-The Role of Quenched-in Vacancies. Applied Surface Science 255: 132-135 (2008).

[Wam78] W.R. Wampler and W.B. Gauster. Positron Annihilation Studies of Quenched Aluminium. J. Phys. F: Metal Phys., Vol. 8, No. 1 (1978).

[Wlo07] J.P. Wloka. Korrosionuntersuchnungen an scandiumhaltigen AlZnMgCu-Legierngen unter besonderer Berücksichtigung des Einflusses intermetallischer Phasen. Der Technischen Falkultät der Universität Erlangen-Nürnberg (2007).

[Zam02] C. Zamponi. Positronenspektroskopie an Plastischen Zonen in Al-Legierungen und GaAs-Wafern. Dissertation, Rheinische Friedrich-Wilhelms-Universität Bonn (2002).

[Web1] Wikipedia. http://en.wikipedia.org/
[Web2] Crystal Defects. http://courses.eas.ualberta.ca/eas421/lecturepages/mylonite.html
[Web3] Aluminium Stockholders Association. http://www.asauk.co.uk/aluminium-production.htm
[Web4] AluMATTER. http://www.aluminium.matter.org.uk/
[Web5] Reciclado del Aluminio. http://www.confemetal.es/aseral/recuperacion.htm
[Web6] Japan Aluminium Association. http://www.aluminum.or.jp/basic/alumi-sangyo/hf00.html
[Web7] Structure of $MgZn_2$. http://som.web.cmu.edu/structures/S033-MgZn2.html
[Web8] Athena software package. http://cars9.uchicago.edu/~ravel/software/aboutathena.html
[Web9] FEFF Documentation. http://leonardo.phys.washington.edu/feff/html/documentation.html
[Web10] PAScual. http://sourceforge.net/apps/mediawiki/pascual/index.php?title=Main_Page
[Web11] ATOMS on the Web. http://cars9.uchicago.edu/cgi-bin/atoms/atoms.cgi

Acknowledgments

This thesis work would not have been possible without the support of many people and I would like to convey my sincere thanks to all of them here.

First of all I want to express my gratitude to my supervisor, Prof. Karl Maier who was always helpful and offered very useful suggestions, support and guidance with his copious experience. My heartfelt thanks to Benedikt Klobes for guiding me do the experiments, answering me questions and conscientious corrections of this thesis in the last twelve months, full of patience and zeal.

I have really enjoyed the nice time with all members of our family-like workgroup, thanks to all of you, especially to Osman Balarisiour for the collaboration in laboratory and our “mini Wikipedia” Björn Korff for sharing the simulation results. The supports from Judith Schindler, Anna-Lisa Kofahl and Peter Wolf for guiding my tutorial groups are greatly appreciated, so that I could concentrate my mind to finishing this work.

Dr. Doris Thrun, Dr. Bernard Metsch and Miss Petra Weiss of BIPP program are gratefully acknowleged, without their admission at the beginning and the continuous financial support this study would not have been possible.

I want to give my appreciation to Mr. Achim Henny and Mr. Berhold Kann from the sychtronton radiation group for producing the isotop source, Mrs. Hildegard Hodde for providing the required chemical stuff for the experiments. Many thanks to Sven-Martin Hühne for the EDX measurement, Mrs. Gertrud Dittmann and Mr. Dominik Thönnes from Institute of Inorganic Chemistry for the supplement of dry ice. All colleagues from the fine mechanical and electronic workshop are sincerely acknowledged for their invaluable help.

I would also like to convey thanks to PD Dr. Torsten Staab for his support about the XAS measurement, Dr. Esther Dudzik and Dr. Ralf Feyerherm from BESSY for providing their enthusiastic help as well as the laboratory facilities.

Finally I wish to express my deepest love to my beloved families and friends for their understanding and endless love through the duration of my study. Particular thankfulness to my dear grandma in Germany: Prof. Sabina Kowalewski who takes care of me all the time and makes me feel home in this foreign country.

Appendix

A.1. Properties of Aluminium

Physical Properties	
Phase	solid
Density (near r.t.)	2.70 g·cm^{-3}
Liquid density at m.p.	2.375 g·cm^{-3}
Melting point	933.47 K660.32 ° ,C1220.58 ° ,F
Boiling point	2792 K2519 ° ,C4566 ° ,F
Heat of fusion	10.71 kJ·mol^{-1}
Heat of vaporization	294.0 kJ·mol^{-1}
Specific heat capacity	(25 °C) 24.200 J·mol^{-1}·K^{-1}

Miscellanea	
Crystal structure	face-centered cubic
Magnetic ordering	paramagnetic
Electrical resistivity	(20 °C) 28.2 nΩ·m
Thermal conductivity	(300 K) 237 W·m^{-1}·K^{-1}
Thermal expansion	(25 °C) 23.1 µm·m^{-1}·K^{-1}
Speed of sound	(r.t.) (rolled) 5,000 m·s^{-1}
Young's modulus	70 GPa
Shear modulus	26 GPa
Bulk modulus	76 GPa
Poisson ratio	0.35
Mohs hardness	2.75
Vickers hardness	167 MPa
Brinell hardness	245 MPa
CAS registry number	7429-90-5

A.2. Properties of AA7075

Typical Analysis (Ave. values %)	Mg	Mn	Fe	Si	Zn	Cr	Ti	Cu	Zr+Ti	Al
	2.5	0.3	0.5	0.4	5.5	0.23	0.2	1.6	0.25	88.5
NEAREST STANDARD	BS					ISO				
	EN AW-7075					Al Zn5.5MgCu				

DESCRIPTION	Heat treatable, very high strength alloy. Very high fatigue strength.

APPLICATIONS	Machine parts and tools for rubber and plastic.

MECHANICAL PROPERTIES	Temper	Tensile strength MPa	0.2% Proof stress MPa	Elong.A5 %	Elong.A50 %	Hardness Vickers
	O	225	105	-	17	65
	T6	530-570	460-505	7-10	10	160
	T7	505	435	13	12	150

FABRICATION PROPERTIES		
	Machinability	Excellent
	Extruding	Fair
	General	Fair

PHYSICAL PROPERTIES		
	Density	2.81 (kg/dm^3)
	Melting point (Liquidus)	635°C
	Melting point (Solidus, Eutectic)	475°C
	Coefficient of thermal expansion	23.5-$\mu mm^{-1}K^{-1}$
	Thermal conductivity	134-W $m^{-1}K^{-1}$
	Specific heat capacity	862 JKg^{-1} K^{-1}
	Electrical resistivity	52 nΩ m
	Electrical conductivity	33% IACS

A.3. Crystal Structure Data of η´ and η Precipitates

η- precipitate

- **Unit cell parameters**

A	B	C	α	β	γ
5.2210Å	5.2210 Å	8.5670 Å	90°	90°	120°

- **Atomic coordinates**

spacegroup P63/mmc			
Atom	**X**	**Y**	**Z**
Mg	1/3	2/3	0.0620
Zn (2)	0	0	0
Zn (1)	0.8305	0.6610	0.2500

η´- precipitate

- **Unit cell parameters**

A	B	C	α	β	γ
4.9600Å	4.9600 Å	14.0500 Å	90°	90°	120°

- **Atomic coordinates**

spacegroup P63/mmc			
Atom	**X**	**Y**	**Z**
Zn	0.17	0.34	1/4
Mg	1/3	2/3	0.63
Al	1/3	2/3	0.09
Al	0	0	0.09

A.4. Program for XAS Measurement of Sample 7075_65_3

```
compressor_on
set_temp 173
umv energy 9670
ascan ystage –6 9 75 1
umv ystage –3.1
ct
umv s3vg 0.14
ct→111322
ascan energy 9690 9630 120 1
umv ystage 5.6
umv energy 9670
ct
umv s3vg 0.3
ct→110671
dscan tth –3 3 30 1
umv tth 88.9
ct
umv s3vg 0.32
ct→116373
econstq 10345 9500 70 1
qdo macro
**********
umv ystage 5.6

econstq 10345 10145 200 1
econstq 10144 9645 1000 1
econstq 9640 9500 28 1

econstq 10345 10145 200 1
econstq 10144 9645 1000 1
econstq 9640 9500 28 1
**********
compressor_off
set_temp 280
```